Front. Mech. Eng. 2023, 18(3): 46
https://doi.org/10.1007/s11465-023-0762-2

RESEARCH ARTICLE

Non-convex sparse optimization-based impact force identification with limited vibration measurements

Lin CHEN[a,b], **Yanan WANG** (✉)[a,b], **Baijie QIAO**[a,b], **Junjiang LIU**[a,b], **Wei CHENG**[a,b], **Xuefeng CHEN**[a,b]

[a] *National Key Laboratory of Aerospace Power System and Plasma Technology, Xi'an Jiaotong University, Xi'an 710049, China*
[b] *School of Mechanical Engineering, Xi'an Jiaotong University, Xi'an 710049, China*
✉ *Corresponding author. E-mail: yananwang@xjtu.edu.cn (Yanan WANG)*

ABSTRACT Impact force identification is important for structure health monitoring especially in applications involving composite structures. Different from the traditional direct measurement method, the impact force identification technique is more cost effective and feasible because it only requires a few sensors to capture the system response and infer the information about the applied forces. This technique enables the acquisition of impact locations and time histories of forces, aiding in the rapid assessment of potentially damaged areas and the extent of the damage. As a typical inverse problem, impact force reconstruction and localization is a challenging task, which has led to the development of numerous methods aimed at obtaining stable solutions. The classical ℓ_2 regularization method often struggles to generate sparse solutions. When solving the under-determined problem, ℓ_2 regularization often identifies false forces in non-loaded regions, interfering with the accurate identification of the true impact locations. The popular ℓ_1 sparse regularization, while promoting sparsity, underestimates the amplitude of impact forces, resulting in biased estimations. To alleviate such limitations, a novel non-convex sparse regularization method that uses the non-convex ℓ_{1-2} penalty, which is the difference of the ℓ_1 and ℓ_2 norms, as a regularizer, is proposed in this paper. The principle of alternating direction method of multipliers (ADMM) is introduced to tackle the non-convex model by facilitating the decomposition of the complex original problem into easily solvable subproblems. The proposed method named ℓ_{1-2}-ADMM is applied to solve the impact force identification problem with unknown force locations, which can realize simultaneous impact localization and time history reconstruction with an under-determined, sparse sensor configuration. Simulations and experiments are performed on a composite plate to verify the identification accuracy and robustness with respect to the noise of the ℓ_{1-2}-ADMM method. Results indicate that compared with other existing regularization methods, the ℓ_{1-2}-ADMM method can simultaneously reconstruct and localize impact forces more accurately, facilitating sparser solutions, and yielding more accurate results.

KEYWORDS impact force identification, inverse problem, sparse regularization, under-determined condition, alternating direction method of multipliers

1 Introduction

Composite materials are widely used in mechanical engineering fields, especially in aeronautical structures due to their excellent properties such as high specific stiffness and specific strength [1]. However, composite structures often suffer from poor impact resistance [2]. When impacted by foreign objects, such as birds, rocks, and hail, composite structures are prone to barely visible impact damage (BVID) such as debonding and delamination [3]. If not detected promptly, BVID seriously threatens the healthy operation of the structure and even causes irreversible damages [4]. Impact force identification can help quickly determine where impact damage is likely to occur and assess the structural integrity. Therefore, it is indispensable to identify impact forces acting on composite structures, including reconstructing their time histories and localizing force positions. Considering that directly monitoring impact forces at unknown locations with force sensors is not feasible, measurable structural responses are used to solve for impact forces inversely instead [5]. In recent years, numerous approaches have emerged to address this challenging inverse problem of impact force identification [6].

To handle the highly ill-posed inverse problem of

Received February 28, 2023; accepted June 13, 2023

impact force identification, regularization methods are commonly employed [7]. As one of the classical regularization methods, Tikhonov regularization is widely used for the inverse problem. Jacquelin et al. [8] conducted a comparative analysis of the effectiveness of Tikhonov, generalized singular value decomposition, truncated singular value decomposition methods in reconstructing impact forces imposed on an aluminum plate in time domain and stated the condition number of the transfer function is influenced by the position of measuring points. Li and Lu [9] localized impact forces through the Nelder−Mead method and then reconstructed their time histories using Tikhonov regularization on a cantilever beam with two accelerometers. Yan et al. [10] proposed a two-step approach for impact force identification, which involves an outer loop for impact localization using a nonlinear unscented Kalman filter and an inner loop for time history reconstruction using Tikhonov regularization. Although ℓ_2 regularization methods like Tikhonov are simple and easy to use, the identification performance is always poor when dealing with sparse, under-determined sensor placement cases [11]. In addition, when applied to impact force identification, ℓ_2 regularization often identifies false loads in the non-loaded area, resulting in poor identification accuracy [12].

With the increasing focus on sparse regularization methods, some researchers have gradually turned their attention from the traditional ℓ_2 norm to the study of solving cost functions based on the ℓ_1 norm because ℓ_1 regularization methods enforce sparsity by promoting a minimum number of nonzero values in the solution, which is in line with the sparse nature of impact forces in the joint time–space domain. Thus, these sparse methods can work well in the case of under-determined sensor configurations [13]. Because the ℓ_1-norm minimization model is convex, it can be solved by convex algorithms, such as the gradient projection method [14], the interior point method [15], and the iterative soft threshold algorithm [16]. Ginsberg and Fritzen [17] simultaneously identified the impact locations and time histories of impact forces acting on a simple beam structure by a direct deconvolution involving an extended ℓ_1-minimization problem. Qiao et al. [18] developed a general sparse model based on minimizing ℓ_1 norm and accurately reconstructed single- and two-source impact forces imposed on a clamped-free shell structure with the monotonic two-step iterative shrinkage/thresholding algorithm. To address the inherent defect that ℓ_1 regularization underestimates the amplitudes of impact forces, Aucejo and De Smet [19] proposed a novel regularization method based on a space–frequency multiplicative approach considering the sparsity of excitation sources in the space domain and verified this method on a thin simply supported steel beam. Pan and Chen [20] improved the identification accuracy of ℓ_1 regularization by introducing some pseudo forces to simulate the effects of additional mass loading. However, the ability of the ℓ_1 norm to promote sparsity is limited, so the above ℓ_1-norm-based methods perform generally in solving the problem of amplitude underestimation [21].

To alleviate the said limitations of ℓ_1 regularization, some non-convex penalties have also been exploited in recent years to solve inverse problems including impact force identification to enhance sparsity [22–24]. Chartrand and Yin [25] indicated non-convex functions, such as ℓ_p quasi-norm $(0 < p < 1)$, can retrieve sparser solutions with fewer measurements than convex ℓ_1 regularization. Then, Qiao et al. [26] successfully introduced the non-convex ℓ_p-norm regularizer into the impact force identification model, and the non-convex regularization method solved this large-scale inverse problem well, which realized the high-precision reconstruction of impact forces. Aucejo and De Smet [27] introduced a local regularization term $\mathcal{R}(\boldsymbol{f}) = \|\boldsymbol{f}\|_q^q$ (q refers to the norm parameter defined in $\mathbb{R}^{+*}$) into the minimization problem, and $\mathcal{R}(\boldsymbol{f})$ is a sparse term when $q < 1$. Liu et al. [28] used a non-convex penalty to establish an optimization objective function for impact force identification and numerically and experimentally verified it on a stiffened composite structure.

In addition to the non-convex regularization methods above, a non-convex penalty called ℓ_{1-2} which is the difference between the ℓ_1 and ℓ_2 norms, has emerged [29] and has been successfully applied in compressive sensing to achieve the high-precision recovery of sparse signals [30]. As mentioned in Ref. [30], ℓ_{1-2} is better than ℓ_1 in promoting sparsity due to its non-convexity. Therefore, in this contribution, the non-convex ℓ_{1-2} penalty is extended to the impact force identification field. To the best of the authors' knowledge, the ℓ_{1-2} minimization method has never been used to solve the impact force identification problem. Different from compressive sensing, the transfer matrix that needs to be dealt with in the impact force identification problem is a large-scale, non-orthogonal, and ill-conditioned Toeplitz-like matrix [31,32], which directly makes the impact force identification model built with the ℓ_{1-2} penalty more difficult to cope with. This paper mainly focuses on monitoring more impact locations from fewer sensors, which means a large-scale, under-determined inverse problem needs to be solved. To this end, a novel ℓ_{1-2} minimization method for impact force identification is proposed to reconstruct and localize impact forces at unknown impact locations simultaneously in the under-determined case with high accuracy. This method uses the non-convex ℓ_{1-2} penalty to construct the impact force identification model. The alternating direction method of multipliers (ADMM) principle that has advantages in addressing large-scale optimization problems [33] is introduced to solve this large-scale under-determined non-convex model to realize the simultaneous localization and reconstruction of impact force. Moreover, unified algorithms for regularized least square problems are derived under the ADMM framework.

The rest of this paper is organized as follows. Section 2 briefly deduces the modeling problem for impact force identification. Section 3 introduces the framework of ADMM. Section 4 introduces the ADMM algorithms with regularization involving ℓ_1 and ℓ_2 norms and derives the non-convex ℓ_{1-2} sparse regularization method via ADMM. Section 5 carries out numerical verification on a composite plate. Section 6 verifies the ℓ_{1-2} sparse regularization method by means of laboratory experiments on a composite plate. Section 7 concludes this paper.

2 Problem statement

For a linear time-invariant single-input single-output (SISO) dynamic system, the convolution relationship between the response and the excitation can be defined as [34]

$$s(t) = a(t) \otimes f(t) = \int_0^t a(t-\tau) f(t) \mathrm{d}\tau, \tag{1}$$

where $s(t)$ is the system response, $a(t)$ is the impulse response function (IRF), $f(t)$ is the impact force excitation, t is the time, τ is the time delayed operator satisfying $t \geqslant \tau$, and the symbol $\otimes$ represents the convolution operation. This paper assumes $s(t) = a(t) = f(t) = 0$ when $t < 0$.

The continuous convolution model Eq. (1) can be discretized as

$$s(N\Delta t) = \Delta t \sum_{i=1}^{N} a((N-i)\Delta t) f(i\Delta t), \tag{2}$$

where Δt is the sampling interval, i is the looping variable within the summation operation satisfying $1 \leqslant i \leqslant N$, and N is the data length of the discretized IRF. Equation (2) can be further written as

$$\begin{bmatrix} s(\Delta t) \\ s(2\Delta t) \\ \vdots \\ s((N-1)\Delta t) \\ s(N\Delta t) \end{bmatrix} = \Delta t \begin{bmatrix} a(\Delta t) & 0 & \cdots & 0 & 0 \\ a(2\Delta t) & a(\Delta t) & \cdots & 0 & 0 \\ \vdots & \vdots & \vdots & \vdots & \vdots \\ a((N-1)\Delta t) & a((N-2)\Delta t) & \cdots & a(\Delta t) & 0 \\ a(N\Delta t) & a((N-1)\Delta t) & \cdots & a(2\Delta t) & a(\Delta t) \end{bmatrix} \begin{bmatrix} f(\Delta t) \\ f(2\Delta t) \\ \vdots \\ f((N-1)\Delta t) \\ f(N\Delta t) \end{bmatrix}. \tag{3}$$

For convenience, Eq. (3) can be expressed concisely as

$$\boldsymbol{s}_{\mathrm{s}} = \boldsymbol{A}_{\mathrm{s}} \boldsymbol{f}_{\mathrm{s}}, \tag{4}$$

where the response vector for the SISO system $\boldsymbol{s}_{\mathrm{s}} \in \mathbb{R}^N$, the excitation force vector for the SISO system $\boldsymbol{f}_{\mathrm{s}} \in \mathbb{R}^N$, and $\boldsymbol{A}_{\mathrm{s}} \in \mathbb{R}^{N\times N}$ refers to the transfer matrix between a single-point excitation force and a single-point response.

The response of a certain measurement position is the linear superposition of the impact force applied at each location, which is described as

$$\boldsymbol{s}_i = \begin{bmatrix} \boldsymbol{A}_{i1} & \boldsymbol{A}_{i2} & \cdots & \boldsymbol{A}_{in} \end{bmatrix} \begin{bmatrix} \boldsymbol{f}_1 \\ \boldsymbol{f}_2 \\ \vdots \\ \boldsymbol{f}_n \end{bmatrix}, \tag{5}$$

where $\boldsymbol{s}_i$ refers to the response at a certain position i.

When impact forces are imposed on several unknown locations over a structure, the responses from several different positions are synchronously recorded as

$$\begin{bmatrix} \boldsymbol{s}_1 \\ \boldsymbol{s}_2 \\ \vdots \\ \boldsymbol{s}_m \end{bmatrix} = \begin{bmatrix} \boldsymbol{A}_{11} & \boldsymbol{A}_{12} & \cdots & \boldsymbol{A}_{1n} \\ \boldsymbol{A}_{21} & \boldsymbol{A}_{22} & \cdots & \boldsymbol{A}_{2n} \\ \vdots & \vdots & \vdots & \vdots \\ \boldsymbol{A}_{m1} & \boldsymbol{A}_{m2} & \cdots & \boldsymbol{A}_{mn} \end{bmatrix} \begin{bmatrix} \boldsymbol{f}_1 \\ \boldsymbol{f}_2 \\ \vdots \\ \boldsymbol{f}_n \end{bmatrix}, \tag{6}$$

where m and n are the number of measurement responses and impact force excitations, respectively.

Equation (6) can also be expressed compactly as

$$\boldsymbol{s} = \boldsymbol{A}\boldsymbol{f} + \boldsymbol{e}, \tag{7}$$

where the response vector $\boldsymbol{s} \in \mathbb{R}^{mN}$, the force vector $\boldsymbol{f} \in \mathbb{R}^{nN}$, the block Topelitz-like matrix $\boldsymbol{A} \in \mathbb{R}^{mN\times nN}$, and the vector $\boldsymbol{e} \in \mathbb{R}^{mN}$ represents random noise and accounts for measurement errors inevitable during the actual measurement. According to the relationship between the amount of measurements m and excitations n, the inverse problem of impact force identification is classified into three categories:

(I) If $m > n$, the inverse problem is under an over-determined condition.

(II) If $m = n$, the inverse problem is under an even-determined condition.

(III) If $m < n$, the inverse problem is under an under-determined condition.

Considering that to be greater than or equal to the number of potential impact locations n in practical applications is sometimes unrealistic for the number of sensors m [35], this paper mainly studies the inverse problem under the under-determined condition. Once the solution $\boldsymbol{f}$ is obtained, the time history reconstruction and localization of the impact force can be achieved simultaneously. If the challenging problem of impact force identification in the under-determined case is solved, then solving the two other cases becomes straightforward.

Under the under-determined condition, the impact force identification problem in Eq. (7) is a typical ill-conditioned problem. Transfer matrix $\boldsymbol{A}$ has a remarkably high condition number, so the inevitable noise in the response causes a large error in the solution result. Therefore, regularization techniques are often resorted to for the stability of solutions. Then, solving $\boldsymbol{f}$ is transformed into solving the general minimization problem,

$$\arg\min_{f} \frac{1}{2}\|\boldsymbol{A}\boldsymbol{f}-\boldsymbol{s}\|_2^2+\lambda g(\boldsymbol{f}), \tag{8}$$

where $\|\boldsymbol{A}\boldsymbol{f}-\boldsymbol{s}\|_2^2$ is the data fidelity item, $g(\boldsymbol{f})$ is the penalty term which incorporates prior knowledge, and λ is the regularization parameter. The regularized least square problem is intractable, especially for the non-convex regularized problem. The impact force identification problem poses a challenge to the solution efficiency and accuracy due to the high dimensionality of the transfer matrix involved. Because ADMM has advantages in solving high-dimensional and non-convex optimization problems [33], this type of least square problem with regularizers is solved under the framework of ADMM in the following section.

3 ADMM principle

ADMM is an effective optimization algorithm for solving convex and non-convex optimization problems [36,37]. To solve the complex optimization problem in Eq. (8), ADMM enables decoupling the regularized term from the smooth data fidelity term, providing computational benefits.

According to ADMM, Eq. (8) can be reformulated as

$$\left\{\hat{\boldsymbol{f}},\hat{\boldsymbol{h}}\right\}=\arg\min_{f} \frac{1}{2}\|\boldsymbol{A}\boldsymbol{f}-\boldsymbol{s}\|_2^2+\lambda g(\boldsymbol{h}),$$

$$\text{s.t. } \boldsymbol{f}-\boldsymbol{h}=0, \tag{9}$$

where the additional vector $\boldsymbol{h}$ is introduced for variable splitting, and the vectors $\hat{\boldsymbol{f}}$ and $\hat{\boldsymbol{h}}$ are the estimated $\boldsymbol{f}$ and $\boldsymbol{h}$, respectively. Subsequently, the augmented Lagrangian function can be obtained from Eq. (9) as

$$\arg\min_{f,h} L(\boldsymbol{f},\boldsymbol{h},\boldsymbol{z}) = \arg\min_{f,h} \frac{1}{2}\|\boldsymbol{A}\boldsymbol{f}-\boldsymbol{s}\|_2^2+\lambda g(\boldsymbol{h}) + \frac{\rho}{2}\|\boldsymbol{f}-\boldsymbol{h}\|_2^2+\rho \boldsymbol{z}^{\mathrm{T}}(\boldsymbol{f}-\boldsymbol{h}), \tag{10}$$

where $\boldsymbol{z}$ is a Lagrange multiplier vector and ρ is a positive penalty parameter able to control the convergence rate. Equation (10) can be solved by updating $\boldsymbol{f}$, $\boldsymbol{h}$, and $\boldsymbol{z}$ separately, resulting in the following three sub problems:

$$\boldsymbol{f}^{(k+1)}=\arg\min_{f}\left(\frac{1}{2}\|\boldsymbol{A}\boldsymbol{f}-\boldsymbol{s}\|_2^2+\rho\left(\boldsymbol{z}^{(k)}\right)^{\mathrm{T}}\boldsymbol{f}+\frac{\rho}{2}\left\|\boldsymbol{f}-\boldsymbol{h}^{(k)}\right\|_2^2\right), \tag{11}$$

$$\boldsymbol{h}^{(k+1)}=\arg\min_{h}\left(\lambda g(\boldsymbol{h})+\frac{\rho}{2}\left\|\boldsymbol{f}^{(k+1)}-\boldsymbol{h}+\boldsymbol{z}^{(k)}\right\|_2^2\right), \tag{12}$$

$$\boldsymbol{z}^{(k+1)}=\boldsymbol{z}^{(k)}+\boldsymbol{f}^{(k+1)}-\boldsymbol{h}^{(k+1)}, \tag{13}$$

where the $\boldsymbol{f}$-update step in Eq. (11) and $\boldsymbol{h}$-update step in Eq. (12) can be completed by calculating their proximal operators, and k is the number of iterations. Equation (11) can be solved by considering the proximal operator of $y(\boldsymbol{f})$ which is $y(\boldsymbol{f})=\frac{1}{2\rho}\|\boldsymbol{A}\boldsymbol{f}-\boldsymbol{s}\|_2^2+(\boldsymbol{z}^{(k)})^{\mathrm{T}}\boldsymbol{f}$. Then Eq. (11) can be rewritten as

$$\mathrm{prox}_{y_f}\left(\boldsymbol{h}^{(k)}\right)=\arg\min_{f}\left\{y(\boldsymbol{f})+\frac{1}{2}\left\|\boldsymbol{f}-\boldsymbol{h}^{(k)}\right\|_2^2\right\}. \tag{14}$$

A closed-form solution of proximal operator in Eq. (14) can be calculated as

$$\boldsymbol{f}^{(k+1)}=\left(\boldsymbol{A}^{\mathrm{T}}\boldsymbol{A}+\rho\boldsymbol{I}\right)^{-1}\left(\boldsymbol{A}^{\mathrm{T}}\boldsymbol{s}+\rho\left(\boldsymbol{h}^{(k)}-\boldsymbol{z}^{(k)}\right)\right), \tag{15}$$

where $\boldsymbol{I}$ is the identify matrix with the same dimensions as the matrix $\boldsymbol{A}^{\mathrm{T}}\boldsymbol{A}$. The specific solutions of sub problem Eq. (12) are determined by the choice of the penalty $g(\boldsymbol{h})$, and the derivation is given in the next section.

4 Regularization methods of impact force identification based on ADMM

By choosing different penalties in Eq. (8), different regularization methods can be formulated. In this section, the classic ℓ_2 regularization method and ℓ_1 sparse regularization method are introduced. Furthermore, a novel sparse regularization method based on ℓ_{1-2} minimization is proposed for impact force identification.

4.1 ℓ_2 regularization via ADMM

Substituting the ℓ_2 norm into Eq. (8), the corresponding minimization problem is

$$\arg\min_{f} \frac{1}{2}\|\boldsymbol{A}\boldsymbol{f}-\boldsymbol{s}\|_2^2+\lambda\|\boldsymbol{f}\|_2^2, \tag{16}$$

where $\|\boldsymbol{f}\|_2^2=\sum_{i=1}^{n}|f_i|^2$ denotes the ℓ_2 norm. Thus, Eq. (12) can be updated accordingly as

$$\boldsymbol{h}^{(k+1)}=\arg\min_{h}\left(\lambda\|\boldsymbol{h}\|_2^2+\frac{\rho}{2}\left\|\boldsymbol{f}^{(k+1)}-\boldsymbol{h}+\boldsymbol{z}^{(k)}\right\|_2^2\right). \tag{17}$$

Because Eq. (17) is a differentiable function, taking its partial derivative with respect to $\boldsymbol{h}$ and making it equal to 0 can obtain the $\boldsymbol{h}$-update step as

$$\boldsymbol{h}^{(k+1)}=\frac{\rho\left(\boldsymbol{f}^{(k+1)}+\boldsymbol{z}^{(k)}\right)}{2\lambda+\rho}. \tag{18}$$

Algorithm 1 shows the ℓ_2 regularization via ADMM. Many studies have applied ℓ_2 regularization to the dynamic force identification and achieved good results when selecting appropriate λ parameters [38,39]. However, ℓ_2 regularization is ineffective at solving under-determined cases [11], and when performing impact force identification, spurious forces appear in non-impact regions [40].

Algorithm 1. ℓ_2 regularization via ADMM (ℓ_2-ADMM)

Input: A, s, λ, ρ, iteration termination threshold ε, maximum iteration $N_{\max}$.

Output: $f^{(k+1)}$.

Initialization: $f^{(0)}=\mathbf{0}$, $h^{(0)}=\mathbf{0}$, $z^{(0)}=\mathbf{0}$, $k=0$.

1. **for** $k=0,1,2,\ldots,N_{\max}$ **do**
2. $f^{(k+1)}=\left(A^{\mathrm{T}}A+\rho I\right)^{-1}\left(A^{\mathrm{T}}s+\rho\left(h^{(k)}-z^{(k)}\right)\right)$,
3. $h^{(k+1)}=\rho\left(f^{(k+1)}+z^{(k)}\right)/(2\lambda+\rho)$,
4. $z^{(k+1)}=z^{(k)}+f^{(k+1)}-h^{(k+1)}$,
5. **if** $\left\|f^{(k+1)}-f^{(k)}\right\|_2\leqslant\varepsilon$, $\left\|f^{(k+1)}-h^{(k+1)}\right\|_2\leqslant\varepsilon$, and $\left\|z^{(k+1)}-z^{(k)}\right\|_2\leqslant\varepsilon$,
6. **break for**
7. **end**
8. $k=k+1$,
9. **end**

4.2 ℓ_1 sparse regularization via ADMM

Considering most entries in $\boldsymbol{f}$ are either equal or close to zero, minimizing the regularized linear least square cost function with ℓ_1 norm is a reasonable compromise to induce sparse solutions of Eq. (7), mathematically expressed by introducing the ℓ_1-norm penalty into Eq. (8) as

$$\arg\min_{\boldsymbol{f}}\frac{1}{2}\|\boldsymbol{s}-\boldsymbol{A}\boldsymbol{f}\|_2^2+\lambda\|\boldsymbol{f}\|_1, \tag{19}$$

where $\|\boldsymbol{f}\|_1=\sum_{i=1}^{n}|f_i|$ denotes the ℓ_1 norm. Then, Eq. (12) can be modified as

$$\boldsymbol{h}^{(k+1)}=\arg\min_{\boldsymbol{h}}\left(\lambda\|\boldsymbol{h}\|_1+\frac{\rho}{2}\left\|\boldsymbol{f}^{(k+1)}-\boldsymbol{h}+\boldsymbol{z}^{(k)}\right\|_2^2\right). \tag{20}$$

By specifying $\boldsymbol{w}=\boldsymbol{f}^{(k+1)}+\boldsymbol{z}^{(k)}$ and $g(\boldsymbol{h})=\|\boldsymbol{h}\|_1$, Eq. (20) can be further written as

$$\boldsymbol{h}^{(k+1)}=\arg\min_{z}\left\{\frac{\lambda}{\rho}g(\boldsymbol{h})+\frac{1}{2}\|\boldsymbol{w}-\boldsymbol{h}\|_2^2\right\}. \tag{21}$$

Thus, Eq. (21) can be solved by Ref. [16],

$$\boldsymbol{h}^{(k+1)}=\max\left(0,\quad\left|\boldsymbol{f}^{(k+1)}+\boldsymbol{z}^{(k)}\right|-\frac{\lambda\boldsymbol{c}}{\rho}\right), \tag{22}$$

where the operator $|\cdot|$ refers to the absolute value of each element in the vector, and the vector $\boldsymbol{c}=[\,1\quad 1\quad\cdots\quad 1\,]^{\mathrm{T}}$ has the same dimension as the vector $\boldsymbol{h}$. To sum up, Algorithm 2 shows the ℓ_1 regularization via ADMM.

Many researchers have applied ℓ_1 regularization methods to reconstruct and localize impact forces simultaneously [12,18]. Although ℓ_1 regularization is feasible and widely used for inducing sparse solutions, theory and practice have proven this convex regularization underestimates the amplitude of impact force [21].

Algorithm 2. ℓ_1 sparse regularization via ADMM (ℓ_1-ADMM)

Input: A, s, λ, ρ, iteration termination threshold ε, maximum iteration $N_{\max}$.

Output: $f^{(k+1)}$.

Initialization: $f^{(0)}=\mathbf{0}$, $h^{(0)}=\mathbf{0}$, $z^{(0)}=\mathbf{0}$, $k=0$.

1. **for** $k=0,1,2,\ldots,N_{\max}$ **do**
2. $f^{(k+1)}=\left(A^{\mathrm{T}}A+\rho I\right)^{-1}\left(A^{\mathrm{T}}s+\rho\left(h^{(k)}-z^{(k)}\right)\right)$,
3. $h^{(k+1)}=\max\left(0,\ \left|f^{(k+1)}+z^{(k)}\right|-\frac{\lambda c}{\rho}\right)$,
4. $z^{(k+1)}=z^{(k)}+f^{(k+1)}-h^{(k+1)}$,
5. **if** $\left\|f^{(k+1)}-f^{(k)}\right\|_2\leqslant\varepsilon$, $\left\|f^{(k+1)}-h^{(k+1)}\right\|_2\leqslant\varepsilon$, and $\left\|z^{(k+1)}-z^{(k)}\right\|_2\leqslant\varepsilon$,
6. **break for**
7. **end**
8. $k=k+1$,
9. **end**

4.3 ℓ_{1-2} sparse regularization via ADMM

To enhance the accuracy and sparsity of the solution, a novel non-convex regularizer is introduced as an alternative to the ℓ_1 norm. The cost function with the non-convex regularizer is generally expressed as

$$\min_{\boldsymbol{f}}\frac{1}{2}\|\boldsymbol{A}\boldsymbol{f}-\boldsymbol{s}\|_2^2+\lambda\|\boldsymbol{f}\|_{1-2}, \tag{23}$$

where $\|\boldsymbol{f}\|_{1-2}=\sum_{i=1}^{n}|f_i|-\sqrt{\sum_{i=1}^{n}|f_i|^2}$ is a mixed non-convex penalty combining the ℓ_1 and ℓ_2 norms, f_i is the ith element in the vector $\boldsymbol{f}$. For intuition, the 3D schematic comparison diagrams of ℓ_1 norm, ℓ_2 norm, and ℓ_{1-2} norm and their corresponding contour maps are depicted in Fig. 1. Figures 1(a) and 1(b) show that as the values of x_1 and x_2 decrease, the contour of the ℓ_{1-2} norm approaches the x_1 and x_2 axes, thereby promoting sparsity. Compared with the ℓ_1 norm, the ℓ_{1-2} norm is closer to the axes as ℓ_0 norm, implying the ℓ_{1-2} norm can be a more proper relaxation of ℓ_0 than ℓ_1.

Then Eq. (12) can be derived as

$$\boldsymbol{h}^{(k+1)}=\arg\min_{\boldsymbol{h}}\left(\lambda(\|\boldsymbol{h}\|_1-\|\boldsymbol{h}\|_2)+\frac{\rho}{2}\left\|\boldsymbol{f}^{(k+1)}-\boldsymbol{h}+\boldsymbol{z}^{(k)}\right\|_2^2\right). \tag{24}$$

By defining $\boldsymbol{w}=\boldsymbol{f}^{(k+1)}+\boldsymbol{z}^{(k)}$ and $\Gamma=\lambda/\rho$, Eq. (24) can be solved by the following shrinkage operation [41]:

$$\operatorname{shrink}_{\ell_{1-2}}(\boldsymbol{w},\Gamma)=\begin{cases}\dfrac{\boldsymbol{u}(\|\boldsymbol{u}\|_2+\Gamma)}{\|\boldsymbol{u}\|_2}, & \|\boldsymbol{w}\|_\infty\geqslant\Gamma,\\ \|\boldsymbol{w}\|_\infty\cdot\operatorname{sign}(w_{\max}), & \|\boldsymbol{w}\|_\infty<\Gamma,\end{cases} \tag{25}$$

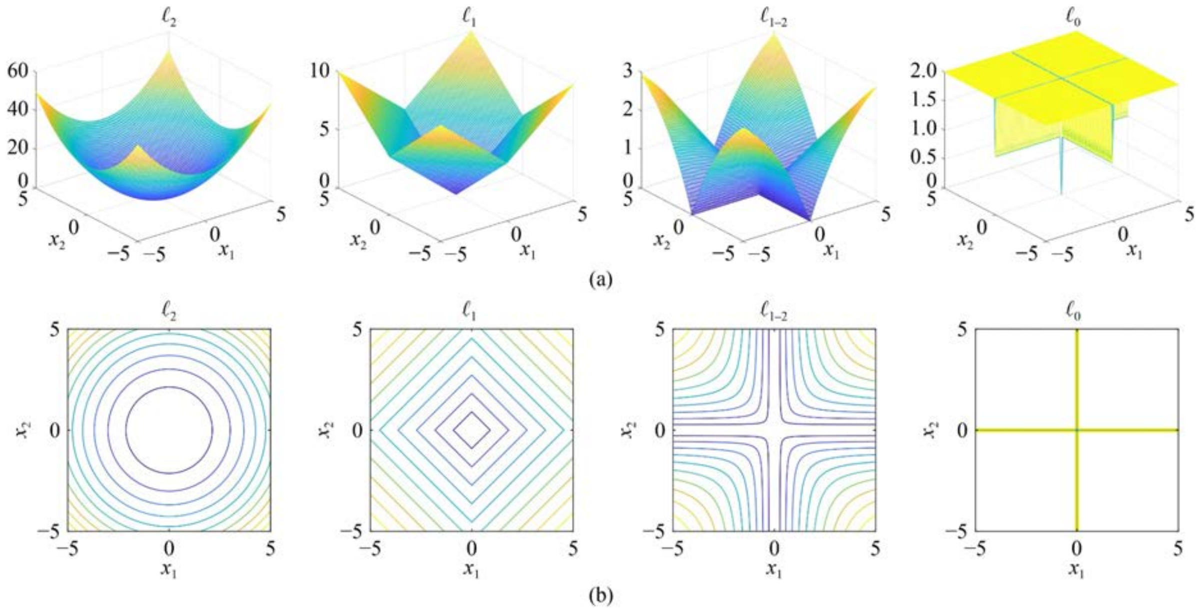

Fig. 1 3D plots of different penalties and their corresponding contour maps: (a) 3D plots of ℓ_2 norm, ℓ_1 norm, ℓ_{1-2} norm, and ℓ_0 norm and (b) corresponding contour maps.

where the vector $\boldsymbol{u}$ is defined as $\boldsymbol{u} = \max(0, |\boldsymbol{w}| - \Gamma \boldsymbol{c})$, and $w_{\max}$ denotes the element with the largest absolute value in vector $\boldsymbol{w}$. Therefore, Algorithm 3 shows the ℓ_{1-2} regularization via ADMM.

Algorithm 3. ℓ_{1-2} sparse regularization via ADMM (ℓ_{1-2}-ADMM)

Input: $\boldsymbol{A}$, $\boldsymbol{s}$, λ, ρ, iteration termination threshold ε, maximum iteration $N_{\max}$.

Output: $\boldsymbol{f}^{(k+1)}$.

Initialization: $\boldsymbol{f}^{(0)} = \boldsymbol{0}$, $\boldsymbol{h}^{(0)} = \boldsymbol{0}$, $\boldsymbol{z}^{(0)} = \boldsymbol{0}$, $k = 0$.

1. **for** $k = 0, 1, 2, \ldots, N_{\max}$ **do**
2. $\boldsymbol{f}^{(k+1)} = \left(\boldsymbol{A}^{\mathrm{T}}\boldsymbol{A} + \rho \boldsymbol{I}\right)^{-1}\left(\boldsymbol{A}^{\mathrm{T}}\boldsymbol{s} + \rho\left(\boldsymbol{h}^{(k)} - \boldsymbol{z}^{(k)}\right)\right)$,
3. $\boldsymbol{h}^{(k+1)} = \mathrm{shrink}_{\ell_{1-2}}\left(\boldsymbol{f}^{(k+1)} + \boldsymbol{z}^{(k)}, \lambda/\rho\right)$,
4. $\boldsymbol{z}^{(k+1)} = \boldsymbol{z}^{(k)} + \boldsymbol{f}^{(k+1)} - \boldsymbol{h}^{(k+1)}$,
5. **if** $\left\|\boldsymbol{f}^{(k+1)} - \boldsymbol{f}^{(k)}\right\|_2 \leqslant \varepsilon$, $\left\|\boldsymbol{f}^{(k+1)} - \boldsymbol{h}^{(k+1)}\right\|_2 \leqslant \varepsilon$, and $\left\|\boldsymbol{z}^{(k+1)} - \boldsymbol{z}^{(k)}\right\|_2 \leqslant \varepsilon$,
6. **break for**
7. **end**
8. $k = k + 1$,
9. **end**

4.4 Computational complexity

According to Ref. [33], a naive method for calculating the $\boldsymbol{f}$-update from Eq. (15) costs $O(n^3N^3 + nN)$ flops, in which $O(\cdot)$ is a symbol used to represent computational complexity, nN is the product of the number of impact excitations and the data length of the discretized IRF. The computational complexity of the $\boldsymbol{h}$-update step and the $\boldsymbol{z}$-update step is $O(nN)$. Therefore, the computational complexity of the three methods based on the ADMM framework is $O(n^3N^3 + nN) + O(nN) + O(nN) \approx O(n^3N^3)$.

5 Numerical validation

In this section, a series of simulations are conducted to evaluate the effectiveness of the proposed ℓ_{1-2}-ADMM method for impact force identification. First, the impact force identification results of ℓ_{1-2}-ADMM, ℓ_1-ADMM, and ℓ_2-ADMM are systematically compared, considering single- and continuous multi-impact cases. Moreover, the effect of noise on the accuracy of the three methods in reconstructing and localizing impact forces is comparatively investigated.

5.1 Problem description

A composite plate with two opposite edges clamped is considered for this numerical validation. The dimensions of this plate are $400\ \mathrm{mm} \times 300\ \mathrm{mm} \times 6\ \mathrm{mm}$, and its material properties are listed in Table 1. The structural dynamics of the plate caused by external impact forces is described by the finite element model in ANSYS. The plate is divided into 16×12 quadratic shell elements, and its first three natural frequencies are 395.88, 441.90, and 621.25 Hz. The Rayleigh damping $\boldsymbol{C} = \alpha \boldsymbol{M} + \beta \boldsymbol{K}$ is considered with $\alpha = 2.6240$ and $\beta = 3.7994 \times 10^{-7}$, where $\boldsymbol{C}$ is the damping matrix, $\boldsymbol{M}$ is the mass matrix, and $\boldsymbol{K}$ is the stiffness matrix.

The employed structural responses used in this numerical validation are strains. The arrangement of strain sensors and potential impact locations for all subsequent simulation studies are shown in Fig. 2, where the optional measurement positions are numbered as $\mathrm{S}_1 - \mathrm{S}_{20}$, and the potential impact locations are sorted as $\mathrm{P}_1 - \mathrm{P}_{15}$. To simulate the under-determined cases, merely

Table 1 Material properties of the composite plate

Elastic modulus	Shear modulus	Poisson's ratio	Density	Layer-ups
$E_1 = 135.0$ GPa,	$G_{12} = 4.47$ GPa,	$v_{12} = 0.3$,		
$E_2 = 8.8$ GPa,	$G_{23} = 3.00$ GPa,	$v_{23} = 0.4$,	$\rho = 1560$ kg/m^3	[45°/0°/−45°/90°]
$E_3 = 8.8$ GPa	$G_{13} = 4.47$ GPa	$v_{13} = 0.3$		

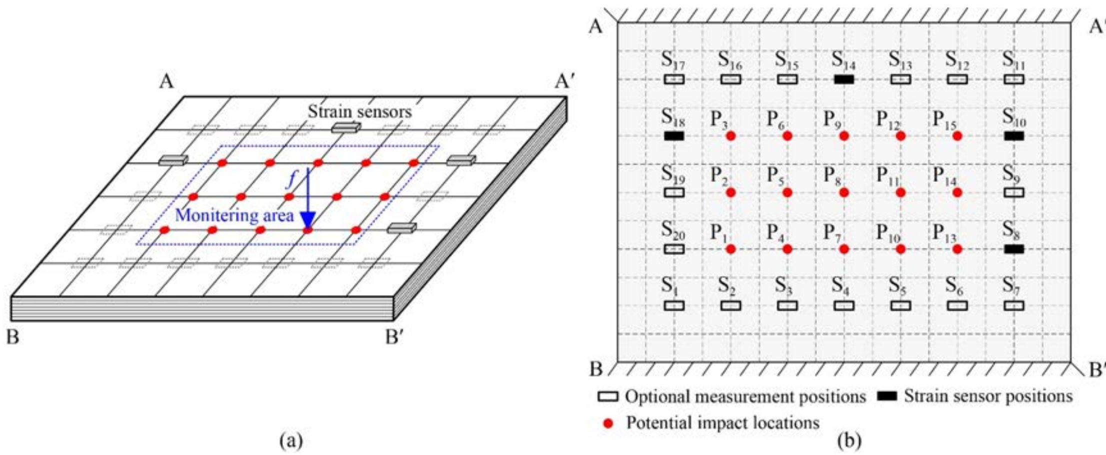

Fig. 2 Composite plate with two opposite edges clamped: (a) schematic diagram of an applied impact force on the plate and (b) distribution of strain sensors and potential impact locations. Fifteen potential impact locations are considered, and the selected measurement positions are S_8, S_{10}, S_{14}, and S_{18}.

four sensors are employed to acquire the responses, as shown in Fig. 2(b). Through the Monte Carlo method, four sensors at S_8, S_{10}, S_{14}, and S_{18} are selected.

In the single-impact case, an impulsive force in the form of Gaussian function is applied perpendicularly to the plate for a very short duration, defined as

$$f_1 = B\mathrm{e}^{-\frac{(t-t_0)^2}{2T^2}}, \tag{26}$$

where B is the amplitude of the impact force, e is the mathematical constant Euler's number, t_0 denotes the occurrence time instant of the impact, and T regulates the impact duration. In the continuous multi-impact case, a composite force combining sine, triangle, and Gaussian impacts is applied vertically to the composite plate.

To simulate actual measured signals, the simulated dynamic responses are corrupted by Gaussian white noise,

$$\tilde{\boldsymbol{s}} = \boldsymbol{s} + \sigma\boldsymbol{r}, \tag{27}$$

where $\tilde{\boldsymbol{s}}$ is the noisy response vector, σ denotes the standard deviation of the vector $\boldsymbol{s}$, and the vector $\boldsymbol{r}$ consists of random values independently drawn from a normal distribution with zero mean and unit standard deviation.

The Green function method with the strain mode shapes of the plate is used to obtain IRF $a(t)$ in advance [42]. The value of the optimal regularization parameter λ is chosen according to the principle of global relative error (GRE) minimization, where GRE is defined as

$$\mathrm{GRE} = \frac{\|\boldsymbol{f} - \hat{\boldsymbol{f}}\|_2}{\|\boldsymbol{f}\|_2} \times 100\%, \tag{28}$$

where $\boldsymbol{f}$ is a column vector composed of actual force vectors at all locations and $\hat{\boldsymbol{f}}$ is composed of estimated ones at all locations. The GRE indicator reflects the global reconstruction accuracy of the method.

To evaluate the reconstruction accuracy at the impact location, the local relative error (LRE) between the actual force vector $\boldsymbol{f}_p$ and the estimated one $\hat{\boldsymbol{f}}_p$ at the impact location can be defined as

$$\mathrm{LRE} = \frac{\|\boldsymbol{f}_p - \hat{\boldsymbol{f}}_p\|_2}{\|\boldsymbol{f}_p\|_2} \times 100\%, \tag{29}$$

where subscript p represents the serial number of the location subjected to impact force.

Moreover, as a local quality indicator for impact force identification, peak relative error (PRE) is defined as

$$\mathrm{PRE} = \frac{\|\max(\boldsymbol{f}_p) - \max(\hat{\boldsymbol{f}}_p)\|_2}{\|\max(\boldsymbol{f}_p)\|_2} \times 100\%. \tag{30}$$

In addition, for the under-determined case, localization error (LE) is required to evaluate the localization accuracy of impact force identification, which is defined as

$$\mathrm{LE} = \left(1 - \frac{\|\hat{\boldsymbol{f}}_p\|_2}{\sum_{i=1}^{n_\mathrm{f}} \|\hat{\boldsymbol{f}}_i\|_2}\right) \times 100\%, \tag{31}$$

where n_f is the total number of potential impact force locations.

For ease of comparison, the iteration termination criteria of the three algorithms need to be consistent, which is described as

$$\frac{\left\|\hat{\boldsymbol{f}}^{(k+1)}-\hat{\boldsymbol{f}}^{(k)}\right\|_1}{\left\|\hat{\boldsymbol{f}}^{(k)}\right\|_1} \leqslant \varepsilon, \tag{32}$$

where the value of ε is set to 10^{-4}.

5.2 Impact force identification using ℓ_{1-2}-ADMM

To assess the performance of the proposed method in identifying single-impact and continuous multi-impact forces, the force reconstruction and localization accuracy of the proposed ℓ_{1-2}-ADMM method are compared with ℓ_1-ADMM and ℓ_2-ADMM methods under the same simulation conditions. The impact force is stochastically applied to a certain location, and the noise level of measurement signals is set to 20 dB. Likewise, to remove randomness, 100 runs are performed independently at each impact location.

For the first case, a single Gaussian impact force is exerted at a random potential impact location on the composite plate. As examples, the identification results of impacts on P_3 and P_{10} are shown in Fig. 3. For the two examples, the computing times for ℓ_{1-2}-ADMM, ℓ_1-ADMM, and ℓ_2-ADMM methods are 243.32, 254.04, and 73.36 s in the P_3 example, respectively, and 265.21, 293.69, and 73.07 s in the P_{10} example, respectively. The amplitude and topography of ℓ_{1-2}-ADMM identification results are closest to the exact forces, whereas ℓ_2-ADMM fails to identify the impact force in the under-determined case despite having the shortest computing time. Figure 4 depicts the comparison of GREs, LREs, PREs, and LEs in the identification results of the three methods at the eight stochastically selected locations. ℓ_{1-2}-ADMM achieves impact force identification with highest accuracy among the three methods, keeping its GREs, LREs, and LEs under 10% and PREs below 5%.

For the second case, a multimorphology continuous-impact force is applied to the plate to verify the performance of ℓ_{1-2}-ADMM further in identifying impacts of different shapes and continuous impacts. Two identification results are given in Figs. 5 and 6 as examples, that is, the multimorphology continuous-impact force is randomly applied to P_9 and P_{11} respectively. ℓ_{1-2}-ADMM can more accurately identify sine, triangle, and Gaussian impacts, and the shapes and peak values of its identification results are most consistent with the exact force, whereas ℓ_2-ADMM still fails to complete the identification task. To provide a more intuitive representation of the identification quality

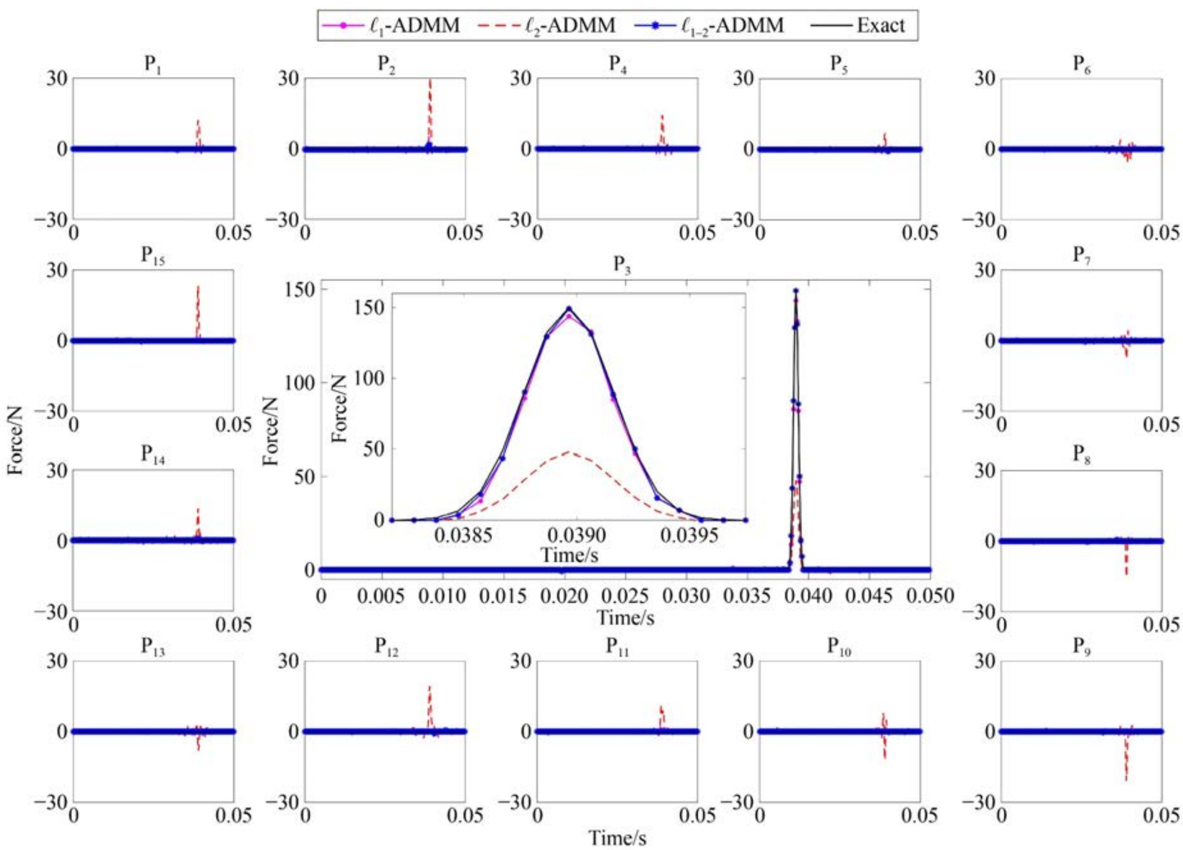

(a)

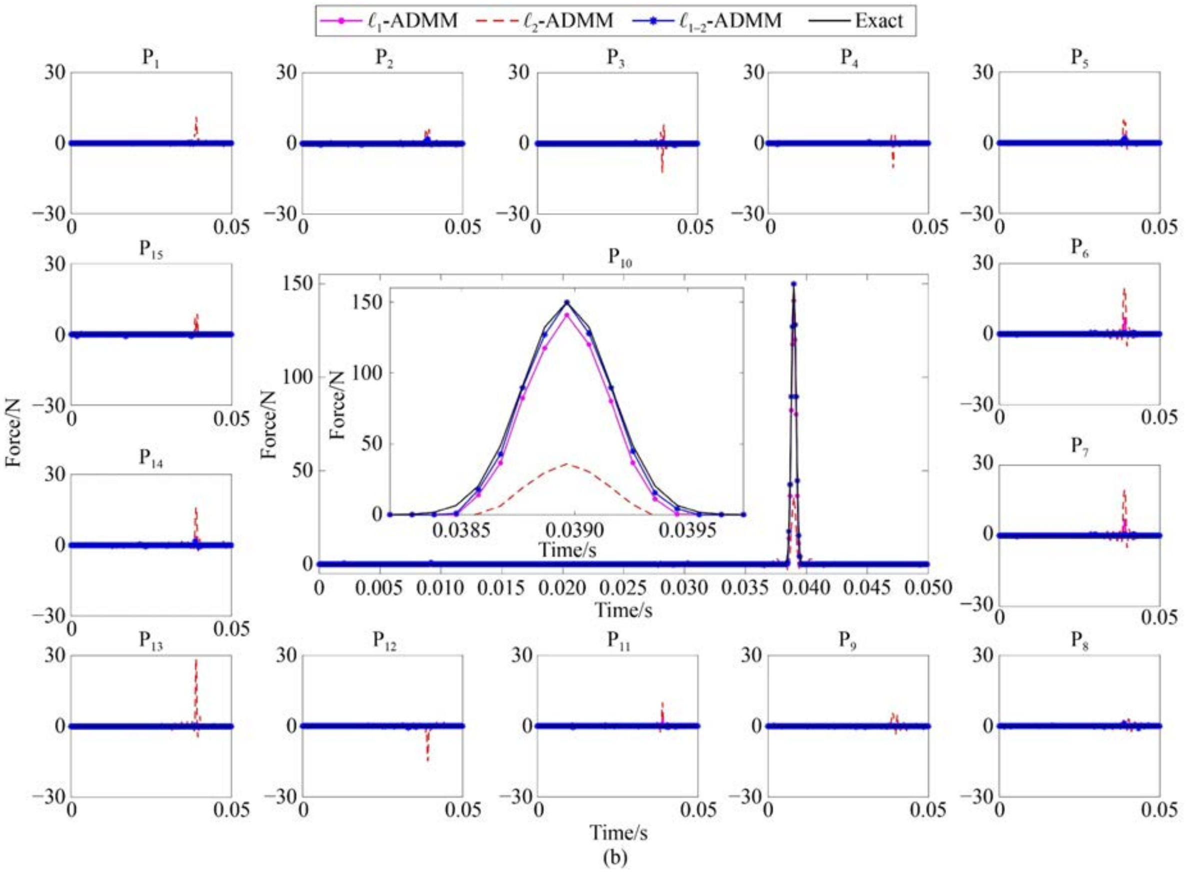

Fig. 3 Reconstructed impact time histories at all monitored locations at 20 dB noise level when (a) real impact acts on P_3 and (b) real impact acts on P_{10}. ADMM: alternating direction method of multipliers.

and computational efficiency of the three methods, the values of the corresponding four accuracy indicators and computing time are listed in Table 2. ℓ_{1-2}-ADMM still maintains the highest identification accuracy and especially improves the identified accuracy of impact amplitudes over ℓ_1-ADMM with similar computing time. Overall, the non-convex ℓ_{1-2}-ADMM method performs the best of the three methods in identifying single-impact forces and multimorphology continuous-impact forces.

5.3 Effect of noise level

To evaluate the robustness of the ℓ_{1-2}-ADMM method under varying noise levels, the performance of the three methods, ℓ_{1-2}-ADMM, ℓ_1-ADMM, and ℓ_2-ADMM, in constructing and localizing the single-impact force randomly imposed at P_1 and P_9 are compared. In this subsection, six different noise levels, namely, 35, 30, 25, 20, 15, and 10 dB, are considered. Similarly, 100 separate

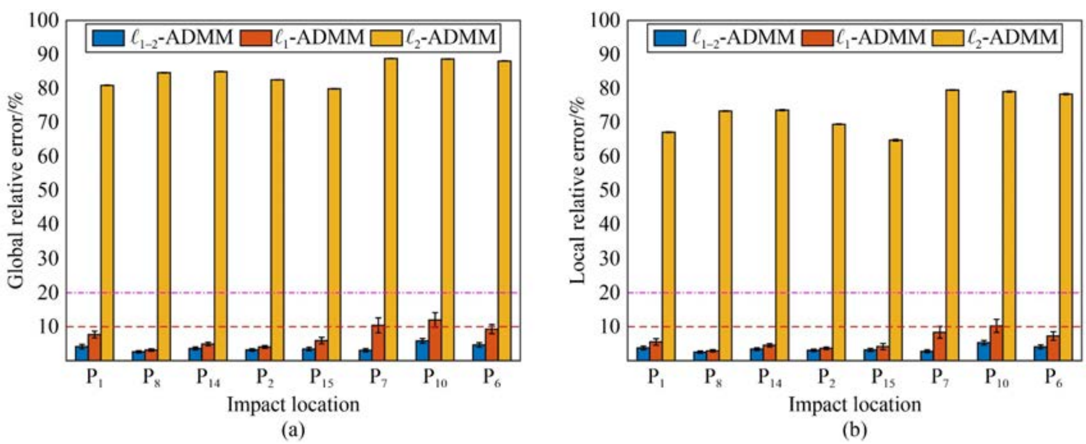

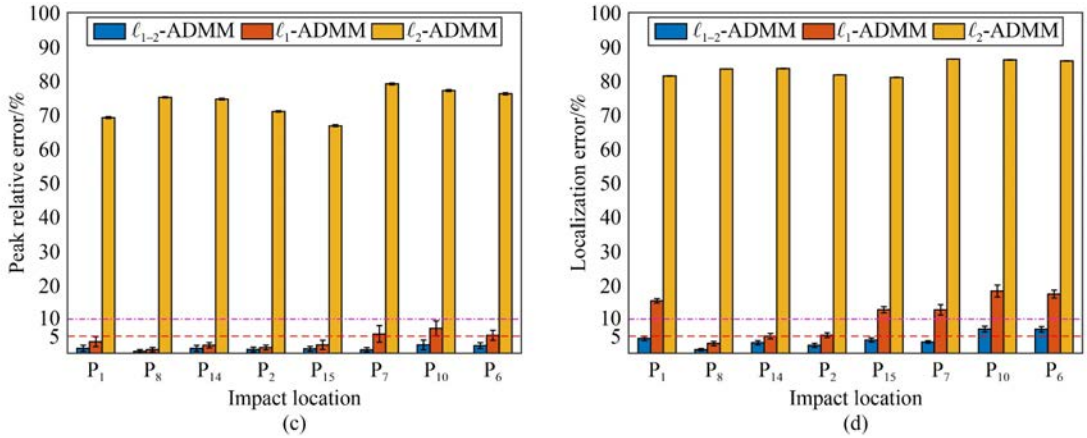

Fig. 4 Impact force identification results denoted by accuracy indicators at eight randomly chosen locations at 20 dB noise level by ℓ_{1-2}-alternating direction method of multipliers (ADMM), ℓ_1-ADMM, and ℓ_2-ADMM: (a) global relative error, (b) local relative error, (c) peak relative error, and (d) localization error.

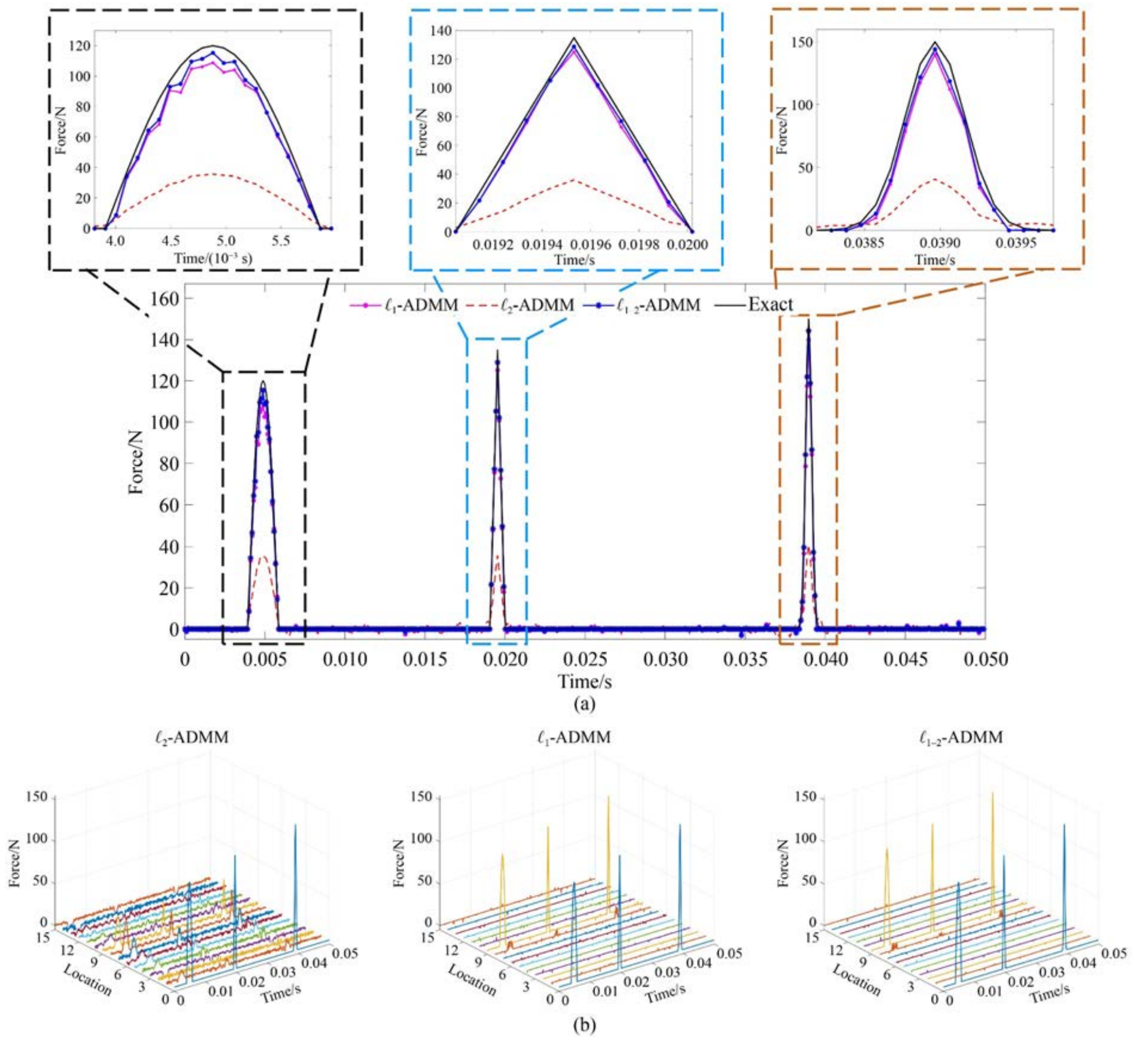

Fig. 5 Identification results of the multimorphology continuous impact force at P_9 under 20 dB noise level by ℓ_{1-2}-alternating direction method of multipliers (ADMM), ℓ_1-ADMM, and ℓ_2-ADMM: (a) time history reconstruction and (b) localization results.

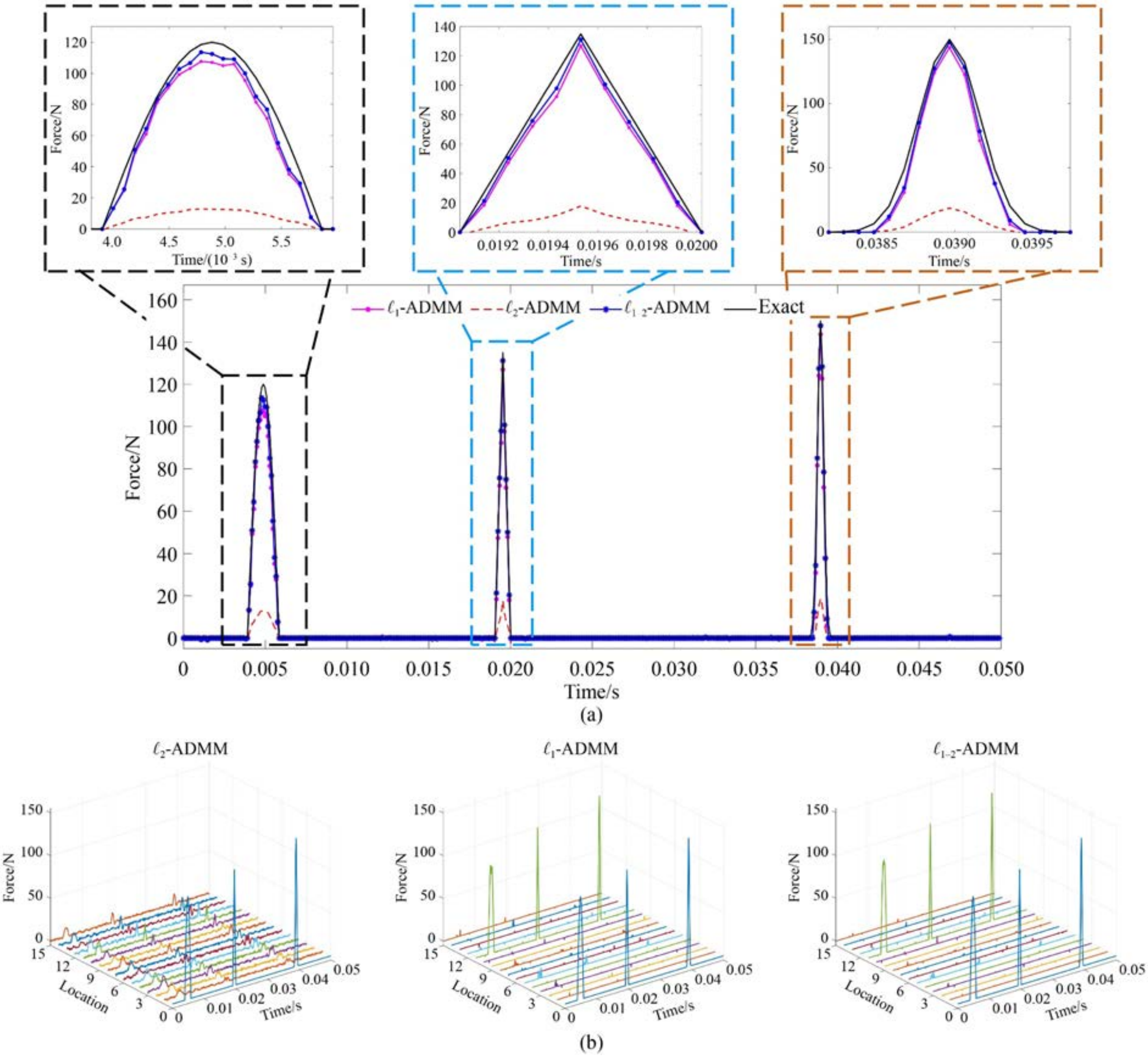

Fig. 6 Identification results of the multimorphology continuous impact force at P_{11} under 20 dB noise level by ℓ_{1-2}-alternating direction method of multipliers (ADMM), ℓ_1-ADMM, and ℓ_2-ADMM: (a) time–history reconstruction and (b) localization results.

Table 2 Identification accuracy indicators and computing time of ℓ_{1-2}-ADMM, ℓ_1-ADMM, and ℓ_2-ADMM for the multimorphology continuous impact force at different locations at 20 dB noise level

Position	Method	GRE/%	LRE/%	PRE/%			LE/%	Computing time/s
				Sine	Triangle	Gaussian		
P_9	ℓ_{1-2}-ADMM	**10.53**	**8.64**	**3.89**	**4.58**	**3.85**	**15.45**	**280.07**
	ℓ_1-ADMM	15.03	11.94	9.33	7.37	6.69	21.92	292.65
	ℓ_2-ADMM	85.90	71.88	70.29	73.42	72.85	84.48	96.88
P_{11}	ℓ_{1-2}-ADMM	**11.03**	**9.59**	**5.35**	**2.80**	**1.49**	**16.11**	272.45
	ℓ_1-ADMM	15.14	13.21	10.30	5.98	4.21	20.78	273.10
	ℓ_2-ADMM	94.21	88.95	89.29	86.83	87.50	90.85	40.14

runs are conducted at each noise level to avoid randomness.

Figure 7 demonstrates the relationships between the accuracy indicators (GREs, LREs, PREs, and LEs) and noise levels when impacting the two locations. ℓ_{1-2}-ADMM holds the highest reconstruction and localization accuracy at various noise levels. Additionally, Fig. 7 indicates the identification accuracy of ℓ_{1-2}-ADMM decreases with the noise increasing, whereas GREs and LREs remain below 10%, and PREs generally keep

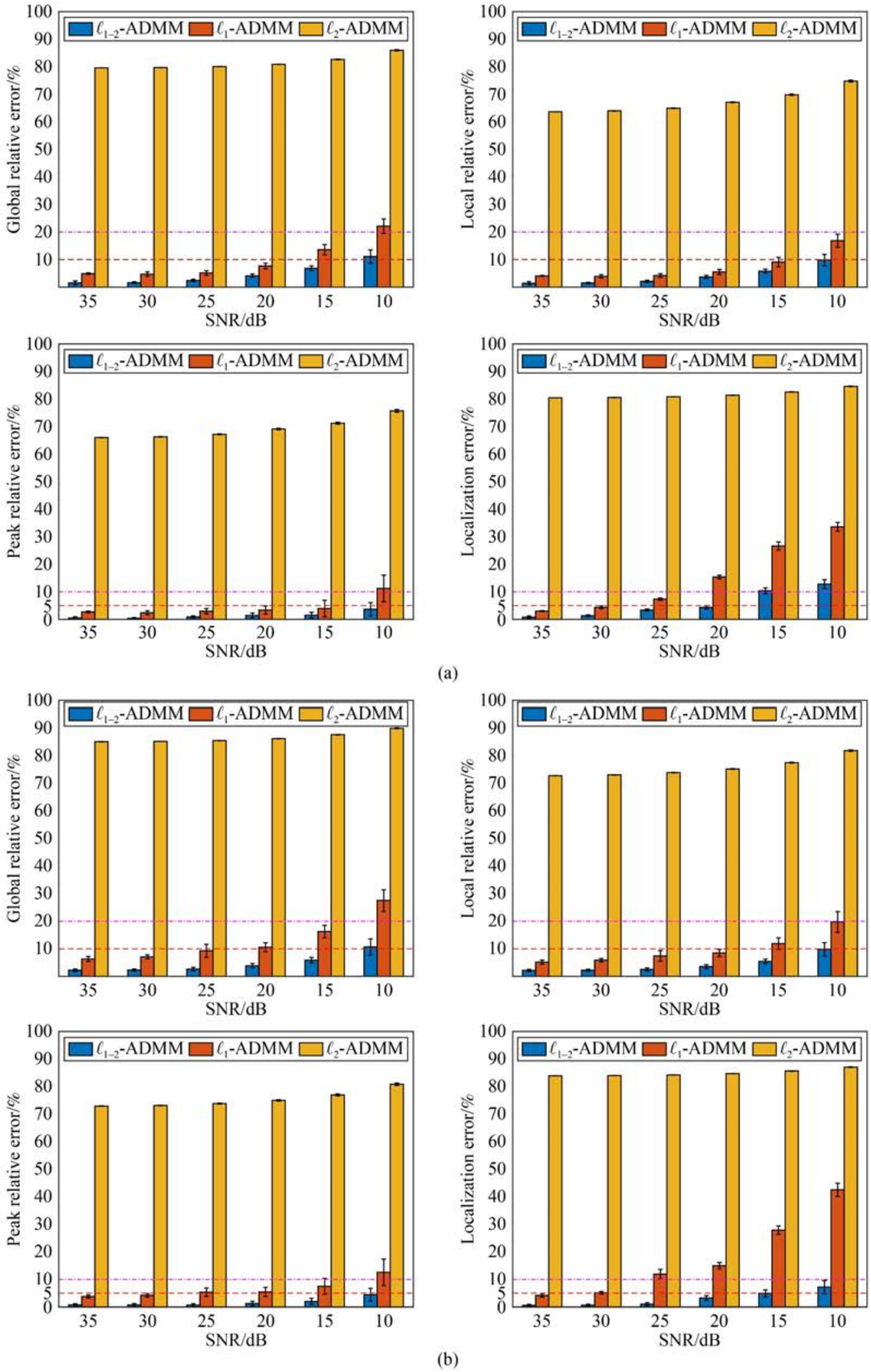

Fig. 7 Four accuracy indicators of identification results for the same single impact force via ℓ_{1-2}-alternating direction method of multipliers (ADMM), ℓ_1-ADMM, and ℓ_2-ADMM at different noise levels: (a) impact at P_1 and (b) impact at P_9. SNR: signal-noise ratio.

below 5% over a range of noise levels from 35 to 10 dB. The LEs of the ℓ_{1-2}-ADMM identification results are kept less than 10% overall during the process of increasing noise and only slightly increase when signal-noise ratio is lower than 15 dB. Generally, ℓ_{1-2}-ADMM performs better than ℓ_1-ADMM and ℓ_2-ADMM at various noise levels, showing the proposed method is quite robust to noise.

6 Experimental verification

In this section, an experimental verification is performed on a composite plate to verify the performance of ℓ_{1-2}-ADMM further in terms of improving accuracy for impact force reconstruction and localization in single- and continuous-impact cases. In addition, compared with the ℓ_1-ADMM and ℓ_2-ADMM methods, the performance of ℓ_{1-2}-ADMM is compared with that of the classic non-convex $\ell_{1/2}$ regularization and $\ell_{2/3}$ regularization methods in terms of impact force identification under the ADMM framework. The $\ell_{1/2}$ regularization and $\ell_{2/3}$ regularization algorithms are detailed in Refs. [43,44]. An under-determined case with limited strain gages same as simulations is considered here, that is, four strain gages are used to monitor 15 potential impact locations, so that the dimension of the transfer matrix $\boldsymbol{A}$ in the experiment is consistent with the simulation.

6.1 Experimental set-up

The configuration of an opposite-side-clamped composite plate with the same parameters and properties as the simulation model is shown in Fig. 8. Impact forces are imposed by an impact hammer (PCB 086C03), and the force sensor embedded in the hammer head measures the impulsive signals. Strain responses are acquired from strain sensors (PCB 740B02). LMS SCADASIII data acquisition system simultaneously records force and strain signals with a sampling frequency of 10240 Hz. Potential impact positions are sorted as P_1–P_{15}, and strain sensor locations are labelled as S_1–S_{10}.

Referring to the simulation study, the strain responses at S_1, S_2, S_7, and S_9 are selected to monitor all 15 potential impact positions. Frequency response function $a_{ij}(\omega)$ between the output position i and the input location j is obtained by performing impact testing via the Lifecycle Management Software modal testing module, and IRF $a_{ij}(t)$ calculated by inverse fast fourier transform of $a_{ij}(\omega)$ is discretized to form the Toeplitz matrix. Same as the simulation, the data analysis length N is 512, resulting in an under-determined system with a dimension of 2048×7680.

6.2 Results and discussion

In the experimental validation, instead of minimizing the

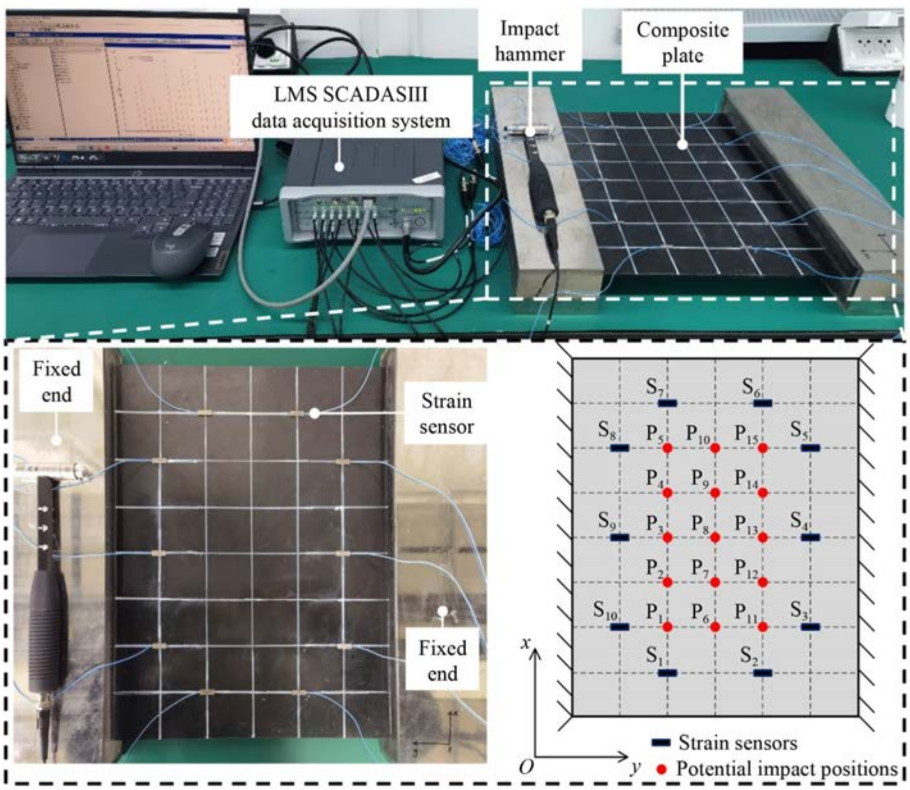

Fig. 8 Experimental setup of the composite plate with two opposite edges clamped. Four sensors (S_1, S_2, S_7, and S_9) are selected to monitor the 15 potential impact locations

GRE value that is infeasible in practice, the λ values of the three methods are chosen by the Monte Carlo generalized stein unbiased risk estimate (MC-GSURE) technique, which is defined as [45]

$$E\left(\|\boldsymbol{Q}(x_\lambda(\boldsymbol{u})-\boldsymbol{f})\|^2\right)=\|\boldsymbol{Q}\boldsymbol{f}\|^2+\|\boldsymbol{Q}x_\lambda(\boldsymbol{u})\|^2 +2\mathrm{div}_{\boldsymbol{u}}(\boldsymbol{Q}x_\lambda(\boldsymbol{u}))-2x_\lambda^{\mathrm{T}}(\boldsymbol{u})\hat{\boldsymbol{f}}_{\mathrm{ML}}, \tag{33}$$

where $\boldsymbol{Q}:=\boldsymbol{A}^{\mathrm{T}}\left(\boldsymbol{A}\boldsymbol{A}^{\mathrm{T}}\right)^{-1}\boldsymbol{A}$ is a projection matrix, $x_\lambda(\boldsymbol{u})$ returns the solution result of Eq. (8), $\boldsymbol{u}=(1/\sigma_n^2)\boldsymbol{A}^{\mathrm{T}}\boldsymbol{s}$ represents the sufficient statistic of the model Eq. (8), σ_n is the standard deviation of noise that can be obtained via the mean absolute derivative method [46], $\hat{\boldsymbol{f}}_{\mathrm{ML}}=\boldsymbol{A}^{\mathrm{T}}\left(\boldsymbol{A}\boldsymbol{A}^{\mathrm{T}}\right)^{-1}\boldsymbol{s}$ denotes the maximum likelihood estimation of the vector $\boldsymbol{f}$, and the divergence $\mathrm{div}_{\boldsymbol{u}}(\boldsymbol{Q}x_\lambda(\boldsymbol{u}))$ is approximated by the Monte Carlo method, which is derived as

$$\mathrm{div}_{\boldsymbol{u}}(\boldsymbol{Q}x_\lambda(\boldsymbol{u}))\approx\boldsymbol{r}^{\mathrm{T}}\boldsymbol{Q}\frac{x_\lambda(\boldsymbol{u}+\delta\boldsymbol{r})-x_\lambda(\boldsymbol{u})}{\delta}, \tag{34}$$

where δ is a small positive parameter set to 10^{-6} [47].

For the single-impact case, impact forces randomly imposed at P_1 and P_{15} are taken as examples. Figure 9 shows the optimal λ values of ℓ_{1-2}-ADMM are selected according to the MC-GSURE criterion, as are other methods and other cases. Figures 10 and 11 depict the time history reconstruction and localization results of the impact forces and iterative convergence curves of the five considered methods. Table 3 lists the GREs, LREs, PREs, and LEs of the identification results and the computing time of these methods. The reconstruction results of ℓ_{1-2}-ADMM best match the shapes of real forces with the least GREs, LREs, PREs, and LEs, and ℓ_2-ADMM is unable to reconstruct and localize the forces. The PREs of ℓ_{1-2}-ADMM are reduced by 76.82% at P_1 and 73.65% at P_{15} compared with ℓ_1-ADMM. The improvement in accuracy of the ℓ_{1-2}-ADMM method for single-impact force identification is relatively slighter compared with that of the $\ell_{1/2}$ and $\ell_{2/3}$ regularization methods. However, the iterations of ℓ_{1-2}-ADMM are much smaller than that of the two other methods, which makes its computing time

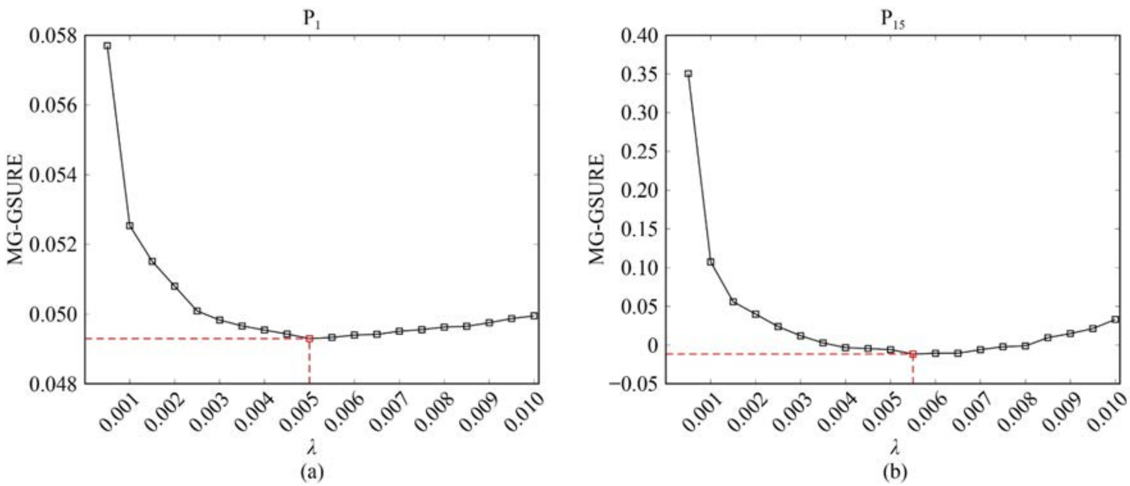

Fig. 9 Monte Carlo generalized stein unbiased risk estimate (MC-GSURE) curves of ℓ_{1-2}-alternating direction method of multipliers in single-impact cases when exerted at: (a) P_1 and (b) P_{15}.

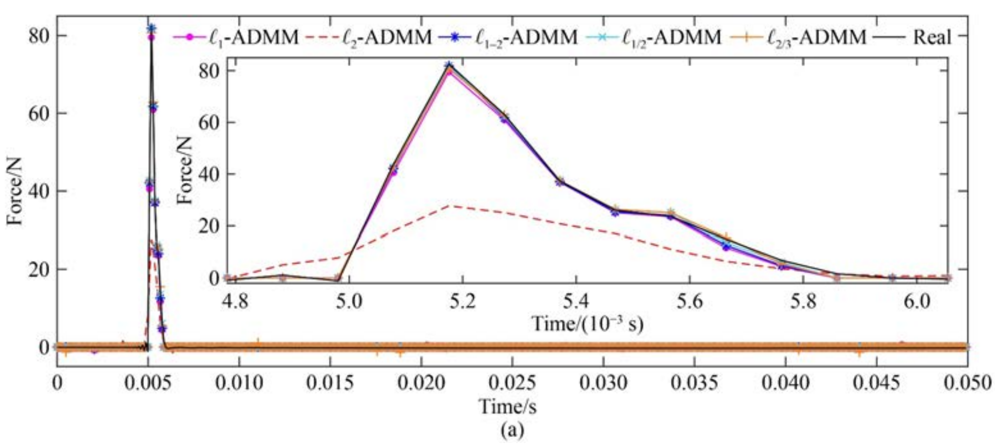

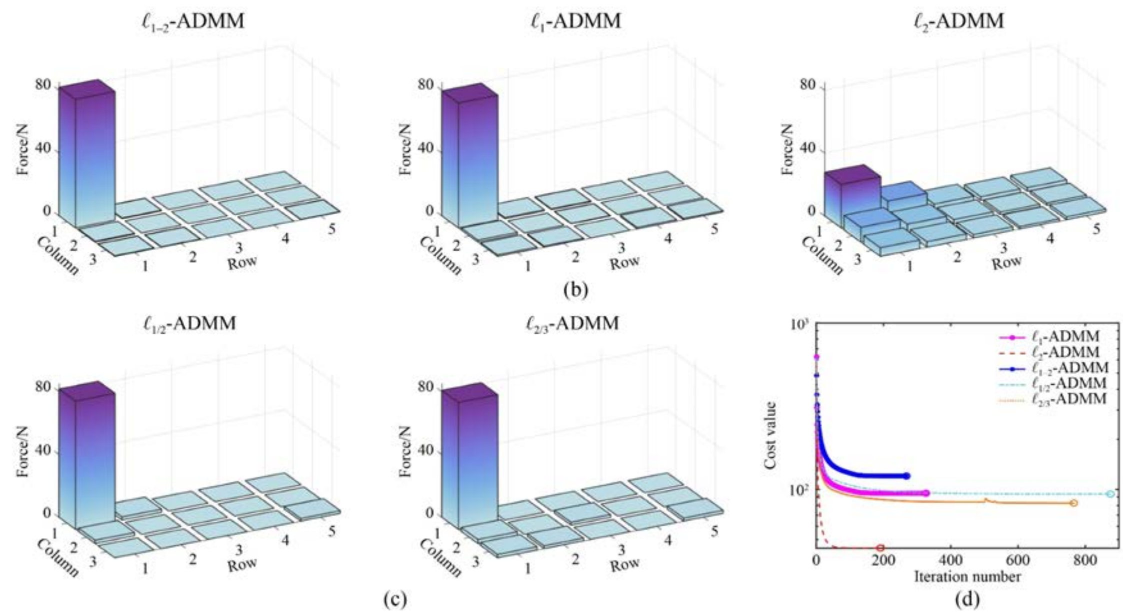

Fig. 10 Identification results of the impact force applied to P_1 by ℓ_{1-2}-alternating direction method of multipliers (ADMM), ℓ_1-ADMM, ℓ_2-ADMM, $\ell_{1/2}$-ADMM, and $\ell_{2/3}$-ADMM: (a) time history reconstruction results, (b) localization results of ℓ_{1-2}-ADMM, ℓ_1-ADMM, and ℓ_2-ADMM, (c) localization results of $\ell_{1/2}$-ADMM and $\ell_{2/3}$-ADMM, and (d) convergence curves.

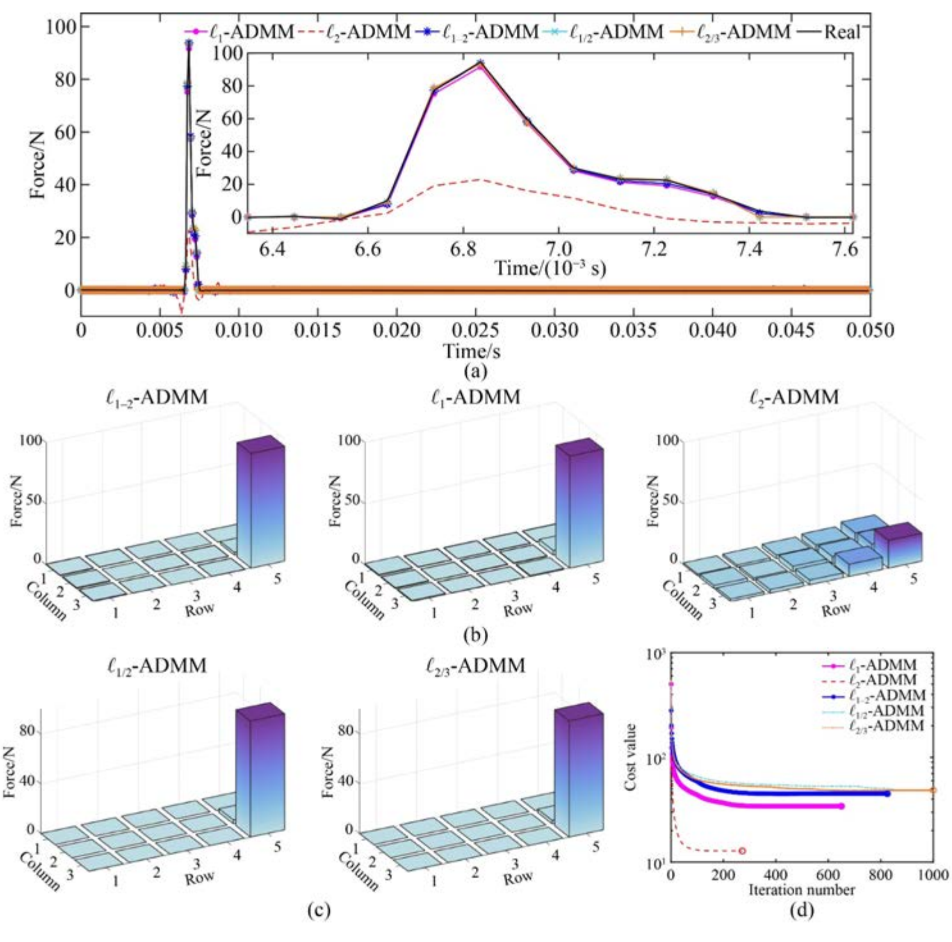

Fig. 11 Identification results of the impact force applied to P_{15} by ℓ_{1-2}-alternating direction method of multipliers (ADMM), ℓ_1-ADMM, ℓ_2-ADMM, $\ell_{1/2}$-ADMM, and $\ell_{2/3}$-ADMM: (a) time history reconstruction results, (b) localization results of ℓ_{1-2}-ADMM, ℓ_1-ADMM, and ℓ_2-ADMM, (c) localization results of $\ell_{1/2}$-ADMM and $\ell_{2/3}$-ADMM, and (d) convergence curves.

Table 3 Identification accuracy indicators and computing times of ℓ_{1-2}-ADMM, $\ell_{1/2}$-ADMM, $\ell_{2/3}$-ADMM, ℓ_1-ADMM, and ℓ_2-ADMM for the single-impact forces applied to P_1 and P_{15}

Method	Accuracy indicators and computing time									
	Impact at P_1					Impact at P_{15}				
	GRE/%	LRE/%	PRE/%	LE/%	Computing time/s	GRE/%	LRE/%	PRE/%	LE/%	Computing time/s
ℓ_{1-2}-ADMM	**5.99**	**5.90**	**0.86**	**2.26**	**93.83**	**5.28**	**4.63**	**0.83**	**6.16**	**267.35**
$\ell_{1/2}$-ADMM	6.44	5.44	1.15	7.22	253.91	6.15	4.96	1.32	4.56	376.05
$\ell_{2/3}$-ADMM	8.10	5.89	2.23	12.70	261.04	5.92	4.98	1.21	4.04	298.46
ℓ_1-ADMM	7.96	7.27	3.71	8.86	101.11	7.59	6.06	3.15	11.37	217.71
ℓ_2-ADMM	75.89	61.63	66.46	77.97	46.24	86.91	77.31	75.77	83.09	71.51

shorter and its computational efficiency higher.

In the continuous-impact case, impact forces stochastically imposed at P_5 and P_6 are taken as examples. The impact time history reconstruction, localization results, and iterative convergence curves of the five methods are depicted in Figs. 12 and 13. The values of

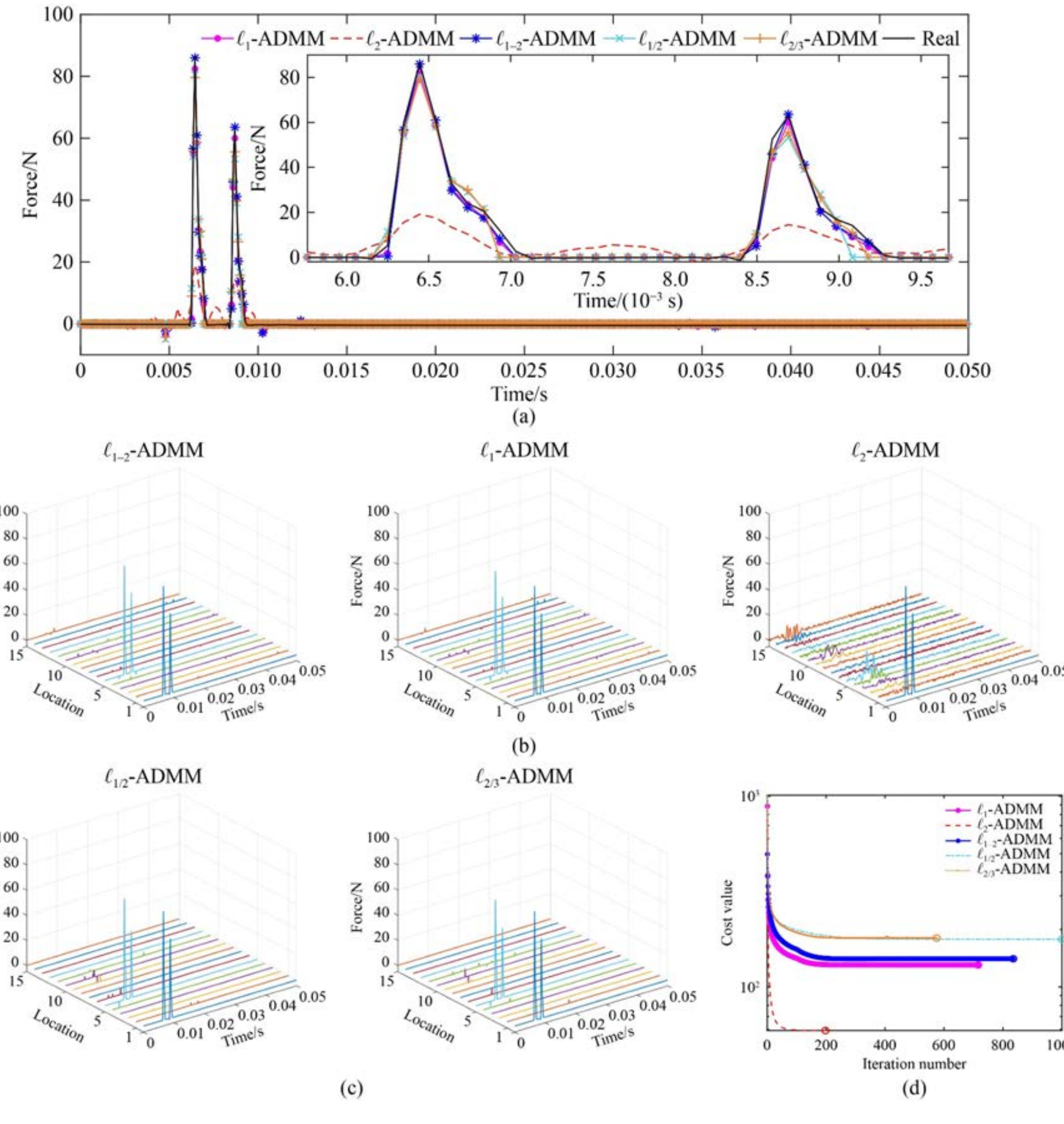

Fig. 12 Identification results of the impact force applied to P_5 by ℓ_{1-2}-alternating direction method of multipliers (ADMM), ℓ_1-ADMM, ℓ_2-ADMM, $\ell_{1/2}$-ADMM, and $\ell_{2/3}$-ADMM: (a) time history reconstruction results, (b) localization results of ℓ_{1-2}-ADMM, ℓ_1-ADMM, and ℓ_2-ADMM, (c) localization results of $\ell_{1/2}$-ADMM and $\ell_{2/3}$-ADMM, and (d) convergence curves.

the accuracy indicators (GREs, LREs, PREs, and LEs) and computing time are presented in Table 4. Figures 12 and 13 show the time history reconstruction results of ℓ_{1-2}-ADMM are still the closest to the amplitudes and

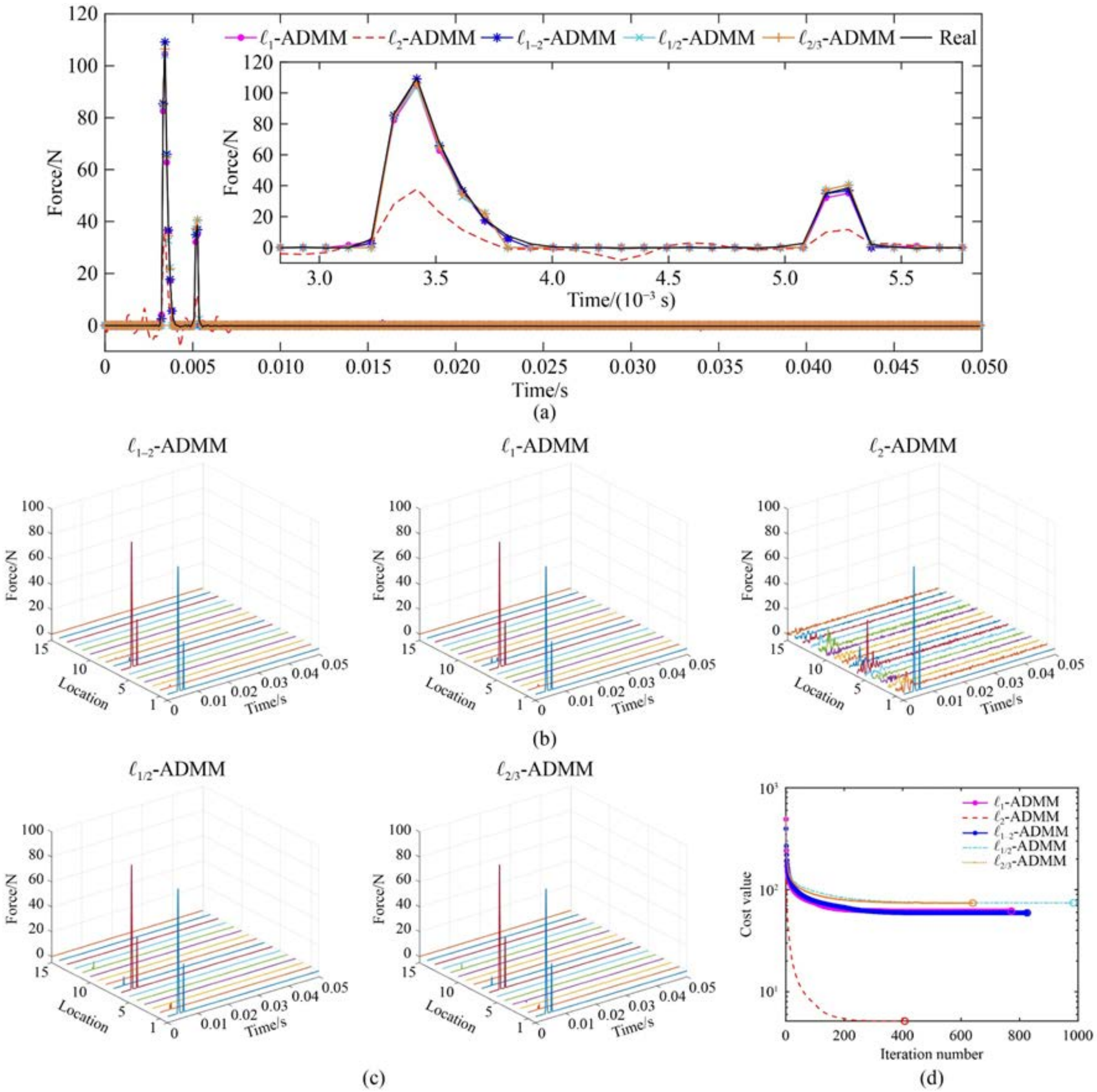

Fig. 13 Identification results of the impact force applied to P_6 by ℓ_{1-2}-alternating direction method of multipliers (ADMM), ℓ_1-ADMM, ℓ_2-ADMM, $\ell_{1/2}$-ADMM, and $\ell_{2/3}$-ADMM: (a) time history reconstruction results, (b) localization results of ℓ_{1-2}-ADMM, ℓ_1-ADMM, and ℓ_2-ADMM, (c) localization results of $\ell_{1/2}$-ADMM and $\ell_{2/3}$-ADMM, and (d) convergence curves.

Table 4 Identification accuracy indicators and computing times of ℓ_{1-2}-ADMM, $\ell_{1/2}$-ADMM, $\ell_{2/3}$-ADMM, ℓ_1-ADMM, and ℓ_2-ADMM for the continuous-impact forces applied to P_5 and P_6

Method	Accuracy indicators and computing time											
	Impact at P_5						Impact at P_6					
	GRE/%	LRE/%	PRE/%		LE/%	Computing time/s	GRE/%	LRE/%	PRE/%		LE/%	Computing time/s
			Peak1	Peak2					Peak1	Peak2		
ℓ_{1-2}-ADMM	**11.76**	**9.88**	**0.48**	**0.93**	**18.17**	**219.71**	**5.94**	**4.95**	**0.40**	**4.29**	**7.76**	**229.85**
$\ell_{1/2}$-ADMM	19.80	17.74	6.84	15.35	15.60	287.43	11.49	8.94	4.88	5.26	11.44	282.67
$\ell_{2/3}$-ADMM	16.46	14.35	7.89	11.67	21.25	188.96	10.17	8.12	2.81	5.17	10.43	193.90
ℓ_1-ADMM	13.57	11.29	4.56	4.71	21.25	189.58	8.53	7.22	4.62	8.83	8.56	213.31
ℓ_2-ADMM	85.39	74.96	77.90	77.02	82.19	45.69	82.20	68.81	65.50	69.85	81.10	101.03

shapes of the exact forces, and its force localization results are most accurate among the three methods. Table 4 presents that ℓ_{1-2}-ADMM holds the lowest GREs, LREs, and PREs. Compared with ℓ_1-ADMM, the PREs of ℓ_{1-2}-ADMM decline by 89.47% and 80.25% at P_5, and decrease by 91.34% and 51.42% at P_6. Moreover, the performance of $\ell_{1/2}$ and $\ell_{2/3}$ regularization methods in identifying continuous impact forces is poor in the two cases.

All the above results show the ℓ_{1-2}-ADMM method performs best in reconstructing and localizing impact forces under the under-determined condition among the five methods, effectively improving the amplitude accuracy and reducing the reconstruction error compared with ℓ_1-ADMM and ℓ_2-ADMM. Moreover, the advantage of ℓ_{1-2}-ADMM over $\ell_{1/2}$ and $\ell_{2/3}$ regularization methods is that it avoids the discussion of the value of q in ℓ_q regularization, and it converges faster during iteration, which improves computational efficiency.

7 Conclusions

In this paper, a novel non-convex sparse regularization method with ℓ_{1-2}-norm is proposed for reconstructing and localizing impact forces from limited structure responses. From an economic feasibility and viability perspective, this work focuses on the case where the monitored structure has a sparse, under-determined sensor arrangement. Instead of convex regularization, a novel non-convex regularization method is considered using the ℓ_1 norm minus the ℓ_2 norm. The ADMM principle is introduced to solve this large-scale, non-convex, and under-determined problem of impact force identification efficiently by decomposing the intractable original problem into easy-to-solve subproblems. Unified algorithms via ADMM for such regularized least square problems are provided.

Simulations and experiments are carried out on a composite plate with two opposite edges clamped, both monitoring 15 potential impact locations with four strain sensors, and the MC-GSURE technique is used in experiments to select appropriate regularization parameters. Based on the simulation and experimental results, the ℓ_{1-2}-ADMM method has higher reconstruction and localization accuracy than ℓ_1-ADMM and ℓ_2-ADMM in single- and continuous-impact cases. Particularly, ℓ_{1-2}-ADMM works very well for improving amplitude accuracy in contrast with ℓ_1-ADMM. ℓ_2-ADMM fails to reconstruct and localize impact forces under the under-determined condition. Additionally, ℓ_{1-2}-ADMM can identify impact forces with different shapes (i.e., sine, triangular, and Gaussian) in simulation, especially its reconstructed triangular and Gaussian impact forces best match the shapes of the exact ones. In this aspect, ℓ_{1-2}-ADMM also performs better than the ℓ_1-ADMM and ℓ_2-ADMM methods. Moreover, the ℓ_{1-2}-ADMM method outperforms ℓ_1-ADMM and ℓ_2-ADMM methods at different impact locations under different noise levels, and its identification results hold the satisfactory GREs, LREs, PREs, and LEs even at 10 dB noise level, which proves ℓ_{1-2}-ADMM is quiet robust to noise. In the experimental verification, the reconstruction accuracy of ℓ_{1-2}-ADMM is slightly higher than that of $\ell_{1/2}$ and $\ell_{2/3}$ regularization. Compared with ℓ_p regularization methods, ℓ_{1-2}-ADMM avoids the need for p-value discussions and reduces the number of iterations, thus improving computational efficiency. All these satisfactory performances of the ℓ_{1-2}-ADMM method demonstrate its potential to solve the impact force identification problem with a sparse sensor configuration in practical engineering applications.

Nomenclature

Abbreviations

ADMM	Alternating direction method of multipliers
BVID	Barely visible impact damage
GRE	Global relative error
IRF	Impulse response function
LE	Localization error
LRE	Local relative error
MC-GSURE	Monte Carlo generalized stein unbiased risk estimate
PRE	Peak relative error
SISO	Single-input single-output
SNR	Signal-noise ratio

Variables

$a(t)$	Impulse response function
$a_{ij}(t)$	Impulse response function between the output position i and the input location j
$a_{ij}(\omega)$	Frequency response function between the output position i and the input location j
$\boldsymbol{A}$	Transfer matrix of the multiple-input multiple-output dynamic system
$\boldsymbol{A}_\mathrm{s}$	Transfer matrix of the single-input single-output dynamic system
B	Amplitude of the Gaussian-shaped impact force
$\boldsymbol{c}$	All-ones vector
$\boldsymbol{C}$	Damping matrix
$\boldsymbol{e}$	Random noise in measurements
E	Elastic modulus
f_i	Elements in the vector $\boldsymbol{f}$

$f(t)$	Impact force excitation function
$\boldsymbol{f}$	Force vector of the multiple-input multiple-output dynamic system
$\hat{\boldsymbol{f}}$	Estimated vector of $\boldsymbol{f}$
$\boldsymbol{f}_p$	Actual force vector at the impact position p
$\hat{\boldsymbol{f}}_p$	Estimated force vector at the impact position p
$\hat{\boldsymbol{f}}_{\mathrm{ML}}$	Maximum likelihood estimation of the vector $\boldsymbol{f}$
$\boldsymbol{f}_{\mathrm{s}}$	Force vector of the single-input single-output dynamic system
$g(\boldsymbol{f})$	General representation function of penalty terms
G	Shear modulus
$\boldsymbol{h}$	An additional vector for variable splitting
$\hat{\boldsymbol{h}}$	Estimated vector of $\boldsymbol{h}$
i	Looping variable within the summation operation
$\boldsymbol{I}$	Identity matrix
k	Number of iterations
$\boldsymbol{K}$	Stiffness matrix
m	Number of measurement responses
$\boldsymbol{M}$	Mass matrix
n	Number of impact force excitations
n_{f}	Total number of potential impact force locations
N	Data length of the discretized impulse response function
$N_{\max}$	Maximum number of iterations
$O(nN)$	Computational complexity of $n \times N$
p	Serial number of the location subjected to impact force
q	Norm parameter defined in $\mathbb{R}^{+*}$
$\boldsymbol{Q}$	Projection matrix
$\boldsymbol{r}$	Gaussian white noise vector
$\mathcal{R}(\boldsymbol{f})$	General expression for calculating the norm of vector $\boldsymbol{f}$
$s(t)$	System response
$\boldsymbol{s}$	Response vector of the multiple-input multiple-output dynamic system
$\tilde{\boldsymbol{s}}$	Noisy response vector
$\boldsymbol{s}_i$	Response vector at a certain position i
$\boldsymbol{s}_{\mathrm{s}}$	Response vector of the single-input single-output dynamic system
t	Time
t_0	Occurrence time instant of the impact
Δt	Sampling interval
T	Impact duration
$\boldsymbol{u}$	Sufficient statistic of the model Eq. (8)
$w_{\max}$	Element with the largest absolute value in the vector·$\boldsymbol{w}$
$\boldsymbol{w}$	Intermediate vector defined as $\boldsymbol{w} = \boldsymbol{f}^{(k+1)} + \boldsymbol{z}^{(k)}$
$x_\lambda(\boldsymbol{u})$	Solution result of Eq. (8) when $\boldsymbol{f} = \boldsymbol{u}$
$y(\boldsymbol{f})$	Proximal operator
δ	Small positive parameter
$\boldsymbol{\delta}$	Lagrange multiplier vector
ε	Iteration termination threshold
λ	Regularization parameter
ρ	A positive penalty parameter
σ	Standard deviation of the vector $\boldsymbol{s}$
σ_n	Standard deviation of noise in the measurements
τ	Time delayed operator
ν	Possion's ratio
Γ	Threshold value defined as $\Gamma = \lambda/\rho$

Acknowledgements This work was supported by the National Natural Science Foundation of China (Grant Nos. 52075414 and 52241502), and China Postdoctoral Science Foundation (Grant No. 2021M702595).

Conflict of Interest The authors declare that they have no conflict of interest.

References

1. Wu J, Xu X B, Liu C, Deng C, Shao X Y. Lamb wave-based damage detection of composite structures using deep convolutional neural network and continuous wavelet transform. Composite Structures, 2021, 276: 114590
2. Gu X J, Su X Z, Wang J, Xu Y J, Zhu J H, Zhang W H. Improvement of impact resistance of plain-woven composite by embedding superelastic shape memory alloy wires. Frontiers of Mechanical Engineering, 2020, 15(4): 547–557
3. Han D, Jia X, Zhang H J, Gao X G, Han X, Sun L, Zheng Z K, Zhang L, Wang F, Song Y D. Foreign object damage and post-impact tensile behavior of plain-woven SiC/SiC composites. Composite Structures, 2022, 295: 115767
4. Singh T, Sehgal S. Structural health monitoring of composite materials. Archives of Computational Methods in Engineering, 2022, 29(4): 1997–2017
5. Chen X F, Wang S B, Qiao B J, Chen Q. Basic research on machinery fault diagnostics: past, present, and future trends. Frontiers of Mechanical Engineering, 2018, 13(2): 264–291
6. Liu R X, Dobriban E, Hou Z C, Qian K. Dynamic load identification for mechanical systems: a review. Archives of Computational Methods in Engineering, 2022, 29(2): 831–863
7. Wang L, Liu Y R, Xu H Y. Review: recent developments in dynamic load identification for aerospace vehicles considering multi-source uncertainties. Transactions of Nanjing University of Aeronautics & Astronautics, 2021, 38(2): 271–287 (in Chinese)
8. Jacquelin E, Bennani A, Hamelin P. Force reconstruction: analysis and regularization of a deconvolution problem. Journal of Sound and Vibration, 2003, 265(1): 81–107
9. Li Q F, Lu Q H. Impact localization and identification under a constrained optimization scheme. Journal of Sound and Vibration,

2016, 366: 133–148
10. Yan G, Sun H, Büyüköztürk O. Impact load identification for composite structures using Bayesian regularization and unscented Kalman filter. Structural Control and Health Monitoring, 2017, 24(5): e1910
11. Aucejo M, De Smet O, Deü J F. On a space-time regularization for force reconstruction problems. Mechanical Systems and Signal Processing, 2019, 118: 549–567
12. Rezayat A, Nassiri V, De Pauw B, Ertveldt J, Vanlanduit S, Guillaume P. Identification of dynamic forces using group-sparsity in frequency domain. Mechanical Systems and Signal Processing, 2016, 70–71: 756–768
13. Candelieri A, Archetti F. Sparsifying to optimize over multiple information sources: an augmented gaussian process based algorithm. Structural and Multidisciplinary Optimization, 2021, 64(1): 239–255
14. Figueiredo M A T, Nowak R D, Wright S J. Gradient projection for sparse reconstruction: application to compressed sensing and other inverse problems. IEEE Journal of Selected Topics in Signal Processing, 2007, 1(4): 586–597
15. Kim S J, Koh K, Lustig M, Boyd S, Gorinevsky D. An interior-point method for large-scale ℓ_1-regularized least squares IEEE Journal of Selected Topics in Signal Processing, 2007, 1(4): 606–617
16. Daubechies I, Defrise M, De Mol C. An iterative thresholding algorithm for linear inverse problems with a sparsity constraint. Communications on Pure and Applied Mathematics, 2004, 57(11): 1413–1457
17. Ginsberg D, Fritzen C P. New approach for impact detection by finding sparse solution. In: Proceedings of ISMA. Leuven: Katholieke Universiteit Leuven, 2014, 2043–2056
18. Qiao B J, Zhang X W, Gao J W, Chen X F. Impact-force sparse reconstruction from highly incomplete and inaccurate measurements. Journal of Sound and Vibration, 2016, 376: 72–94
19. Aucejo M, De Smet O. A space-frequency multiplicative regularization for force reconstruction problems. Mechanical Systems and Signal Processing, 2018, 104: 1–18
20. Pan C D, Chen Z P. Elimination of accelerometer mass loading effects in sparse identification of impact forces. Mechanical Systems and Signal Processing, 2023, 191: 110178
21. Xu Z B, Chang X Y, Xu F M, Zhang H. $L_{1/2}$ regularization: a thresholding representation theory and a fast solver. IEEE Transactions on Neural Networks and Learning Systems, 2012, 23(7): 1013–1027
22. Trehan D. Non-convex optimization: a review. In: Proceedings of 2020 the 4th International Conference on Intelligent Computing and Control Systems. Madurai: IEEE, 2020, 418–423
23. Zha Z Y, Wen B H, Yuan X, Ravishankar S, Zhou J T, Zhu C. Learning nonlocal sparse and low-rank models for image compressive sensing: nonlocal sparse and low-rank modeling. IEEE Signal Processing Magazine, 2023, 40(1): 32–44
24. Zha Z Y, Wen B H, Yuan X, Zhou J T, Zhu C. Image restoration via reconciliation of group sparsity and low-rank models. IEEE Transactions on Image Processing, 2021, 30: 5223–5238
25. Chartrand R, Yin W T. Nonconvex sparse regularization and splitting algorithms. In: Glowinski R, Osher S J, Yin W T, eds. Splitting Methods in Communication, Imaging, Science, and Engineering. Cham: Springer, 2016, 237–249
26. Qiao B J, Ao C Y, Mao Z, Chen X F. Non-convex sparse regularization for impact force identification. Journal of Sound and Vibration, 2020, 477: 115311
27. Aucejo M, De Smet O. A generalized multiplicative regularization for input estimation. Mechanical Systems and Signal Processing, 2021, 157: 107637
28. Liu J J, Qiao B J, Wang Y N, He W F, Chen X F. Non-convex sparse regularization via convex optimization for impact force identification. Mechanical Systems and Signal Processing, 2023, 191: 110191
29. Esser E, Lou Y F, Xin J. A method for finding structured sparse solutions to nonnegative least squares problems with applications. SIAM Journal on Imaging Sciences, 2013, 6(4): 2010–2046
30. Yin P H, Lou Y F, He Q, Xin J. Minimization of ℓ_{1-2} for compressed sensing. SIAM Journal on Scientific Computing, 2015, 37(1): A536–A563
31. Sun H, Feng D M, Liu Y, Feng M Q. Statistical regularization for identification of structural parameters and external loadings using state space models. Computer-Aided Civil and Infrastructure Engineering, 2015, 30(11): 843–858
32. Ginsberg D, Ruby M, Fritzen C P. Load identification approach based on basis pursuit denoising algorithm. Journal of Physics: Conference Series, 2015, 628(1): 012030
33. Boyd S, Parikh N, Chu E, Peleato B, Eckstein J. Distributed optimization and statistical learning via the alternating direction method of multipliers. Foundations and Trends in Machine Learning, 2011, 3(1): 1–122
34. Meirovitch L. Elements of Vibration Analysis. New York: McGraw-Hill Book Co., 1986
35. Jankowski L. Off-line identification of dynamic loads. Structural and Multidisciplinary Optimization, 2009, 37(6): 609–623
36. Zha Z Y, Liu X, Huang X H, Shi H L, Xu Y Y, Wang Q, Tang L, Zhang X G. Analyzing the group sparsity based on the rank minimization methods. In: Proceedings of 2017 IEEE International Conference on Multimedia and Expo. Hong Kong: IEEE, 2017, 883–888
37. Zha Z Y, Zhang X G, Wu Y, Wang Q, Liu X, Tang L, Yuan X. Non-convex weighted ℓ_p nuclear norm based ADMM framework for image restoration Neurocomputing, 2018, 311: 209–224
38. Li X W, Zhao H T, Chen Z, Wang Q B, Chen J A, Duan D P. Force identification based on a comprehensive approach combining Taylor formula and acceleration transmissibility. Inverse Problems in Science and Engineering, 2018, 26(11): 1612–1632
39. Wang L, Liu J K, Lu Z R. Bandlimited force identification based on sinc-dictionaries and Tikhonov regularization. Journal of Sound and Vibration, 2020, 464: 114988
40. Qiao B J, Liu J J, Liu J X, Yang Z B, Chen X F. An enhanced sparse regularization method for impact force identification. Mechanical Systems and Signal Processing, 2019, 126: 341–367
41. Lou Y F, Yan M. Fast L_1–L_2 minimization via a proximal operator. Journal of Scientific Computing, 2018, 74(2): 767–785
42. Chang X T, Yan Y J, Wu Y F. Study on solving the ill-posed problem of force load reconstruction. Journal of Sound and

Vibration, 2019, 440: 186–201

43. Cao W F, Sun J, Xu Z B. Fast image deconvolution using closed-form thresholding formulas of L_q (q = 1/2, 2/3) regularization. Journal of Visual Communication and Image Representation, 2013, 24(1): 31–41
44. Zha Z Y, Yuan X, Wen B H, Zhou J T, Zhang J C, Zhu C. A benchmark for sparse coding: when group sparsity meets rank minimization. IEEE Transactions on Image Processing, 2020, 29: 5094–5109
45. Eldar Y C. Generalized SURE for exponential families: applications to regularization. IEEE Transactions on Signal Processing, 2009, 57(2): 471–481
46. Donoho D L. De-noising by soft-thresholding. IEEE Transactions on Information Theory, 1995, 41(3): 613–627
47. Ramani S, Blu T, Unser M. Monte-carlo sure: a black-box optimization of regularization parameters for general denoising algorithms. IEEE Transactions on Image Processing, 2008, 17(9): 1540–1554